PHYSICAL REVIEW B **67**, 245307 (2003)

Kondo effect in coupled quantum dots: A noncrossing approximation study

Ramón Aguado[1,2,*] and David C. Langreth[2]
[1]*Departamento de Teoría de la Materia Condensada, Instituto de Ciencia de Materiales de Madrid, CSIC, Cantoblanco 28049, Madrid, Spain*
[2]*Center for Materials Theory, Department of Physics and Astronomy, Rutgers University, Piscataway, New Jersey 08854-8019, USA*

(Received 10 July 2002; revised manuscript received 25 March 2003; published 11 June 2003)

The out-of-equilibrium transport properties of a double quantum dot system in the Kondo regime are studied theoretically by means of a two-impurity Anderson Hamiltonian with interimpurity hopping. The Hamiltonian, formulated in slave-boson language, is solved by means of a generalization of the noncrossing approximation (NCA) to the present problem. We provide benchmark calculations of the predictions of the NCA for the linear and nonlinear transport properties of coupled quantum dots in the Kondo regime. We give a series of predictions that can be observed experimentally in linear and nonlinear transport measurements through coupled quantum dots. Importantly, it is demonstrated that measurements of the differential conductance $\mathcal{G}=dI/dV$, for the appropriate values of voltages and interdot tunneling couplings, can give a direct observation of the coherent superposition between the many-body Kondo states of each dot. This coherence can be also detected in the linear transport through the system: the curve linear conductance vs temperature is nonmonotonic, with a maximum at a temperature T^* characterizing quantum coherence between both the Kondo states.

DOI: 10.1103/PhysRevB.67.245307 PACS number(s): 73.63.Kv, 72.15.Qm, 73.23.Hk

I. INTRODUCTION

The recent observations of Kondo physics in the electronic-transport properties of quantum dots (QD's),[1–5] a tiny semiconductor box containing a few interacting electrons,[6] have opened new promising directions for experimental and theoretical research of this phenomenon, one of the paradigms in condensed-matter physics.

The Kondo effect appears in dilute alloys containing localized moments as a crossover from weak to strong coupling between itinerant electrons of the host nonmagnetic metal and the unpaired localized electron of the magnetic impurity as the temperature (T) is reduced well below the Kondo temperature (T_K).[7] Due to spin-exchange interaction, a many-body spin singlet state is formed between the unpaired localized electron and the itinerant electrons with energies close to the Fermi energy of the metal.[8,9] This singlet is reflected in the density of states (DOS) of the impurity as a narrow peak at low frequencies: the Abrikosov-Suhl or Kondo resonance. This effect leads to many remarkable properties and has been the subject of extensive research for decades.[7]

In recent years, spectacular advances in nanotechnology have made it possible to experimentally study Kondo physics in quantum dots.[1–5] These truly impressive experiments confirm early theoretical predictions that transport through quantum dots in the Coulomb blockade regime should exhibit Kondo physics at low enough temperatures.[10] QD's provide the intriguing opportunity to control and modify the Kondo effect experimentally: the continuous tuning of the relevant parameters governing the Kondo effect[7] as well as the possibility of studying Kondo physics when the system is driven out of equilibrium, either by dc (Refs. 11–17) or ac voltages,[18–24] pave the way for the study of strongly correlated electron physics in artificial systems. Moreover, they provide a unique testing ground in which to investigate the interplay of strongly correlated electron physics, quantum coherence, and nonequilibrium physics. More sophisticated configurations of QD's in the Kondo regime constitute a growing area of intense investigations, both from the theoretical and experimental sides. Time-dependent Kondo physics,[25–28] Kondo physics in integer-spin QD's,[29] or QD's embedded in Aharonov-Bohm rings[30] are examples of such configurations.

The study of Kondo physics in mesoscopic or nanoscopic systems is not limited to QD's. We can mention here the recent observation of Kondo physics in single atoms,[31] molecules,[32] carbon nanotubes,[33] scanning tunneling microscopy (STM) experiments of magnetic impurities in quantum corrals[34] or the anomalous energy relaxation in voltage-biased quantum wires and its relation to two-channel Kondo physics.[35]

In this paper, we will focus on another configuration: a system of two coupled quantum dots in the Kondo regime. In view of the recent experimental advances in the study of quantum coherence in coupled quantum dots (DQD)[36–39] and the aforementioned studies of Kondo physics in quantum dots, it is a timely question to ask what happens when a system consisting of two quantum dots in the Kondo regime, coupled to each other by means of a tunneling barrier, is driven out of equilibrium, and how the interplay of strongly correlated electron physics, quantum coherence, and nonequilibrium physics leads to new physical scenarios. Previous theoretical studies of this problem at equilibrium have focused on the aspects of quantum coherence in this system[40,41] and on the competition between the Kondo effect and antiferromagnetic coupling generated via exchange[41–43] or via capacitive coupling between dots.[44] There have hitherto been only few attempts to attack this problem in a nonequilibrium situation by means of different techniques: the equation-of-motion technique,[45] the so-called resonant tunneling approximation[46] (valid for $T>T_K$ and equivalent to the equation-of-motion method of Ref. 12), and slave-boson mean-field theory.[47,48] Here, we present an approach which, to the best of our knowledge, tackles with this nonequilibrium problem in a nonperturbative, fully self-consistent, and

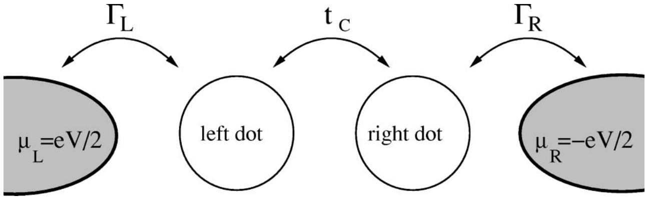

FIG. 1. Schematic diagram of the double-dot system studied in this paper. Each dot is coupled independently to one lead with couplings Γ_L and Γ_R, respectively, t_C is the interdot tunneling term. Note that the role of the interdot term is twofold: first, it generates quantum coherence between the two quantum dots; second, it establishes a nonequilibrium situation, that is, when the chemical potentials are different there is a bias voltage across the system $\mu_L - \mu_R = eV$ and, then, a flow of electrical current through the double-dot system.

conserving way. Our approach is based on a generalization of the so-called ‘‘noncrossing approximation’’ (NCA) (Refs. 49 and 50) to the present problem.

The system of two coupled QD’s can be modeled by means of two Anderson impurities, each of them coupled to a different Fermi sea, and coupled together by means of an interimpurity hopping term. In the atomic limit, each impurity can either be empty $|0\rangle$, singly occupied $|\uparrow\rangle$, $|\downarrow\rangle$ or doubly occupied $|\uparrow\downarrow\rangle$. The operators describing these states and the transitions among them, the Hubbard operators, are neither fermions nor bosons, which precludes the application of usual perturbation theory (Wick’s theorem does not apply). One way of circumventing this difficulty is the auxiliary particle representation pioneered by Abrikosov, who first represented local spins by pseudofermions,[51] and later by Barnes[52] and Coleman[53] and consists of describing each of the states (for each site) as created out of the vacuum from the application of a creation operator (bosonic for $|0\rangle$ and $|\uparrow\downarrow\rangle$ and fermionic for $|\uparrow\rangle$ and $|\downarrow\rangle$ due to quantum statistics). Each site has to be in one of the four states, and this is accomplished by constraining the number of auxiliary particles to 1. Slave-particle representations allow one to work with usual quantum-field-theory methods provided one works in the constrained subspace of the Hilbert space where the number of auxiliary particles is 1. In particular, in the limit $U\rightarrow\infty$ (infinite on-site interaction), which is the case we shall consider in the following, double occupancy is forbidden and each site can be described by one boson $|0\rangle \equiv b^{\dagger}|\text{vac}\rangle$ and two fermions $|\uparrow\rangle \equiv f_{\uparrow}^{\dagger}|\text{vac}\rangle$, $|\downarrow\rangle \equiv f_{\downarrow}^{\dagger}|\text{vac}\rangle$. This particular version of the auxiliary particle representation has been termed the slave-boson (SB) representation after Coleman.[53]

Within the SB formulation two nonperturbative approaches can be applied to N-fold degenerate Anderson-impurity models.

(i) The mean-field approximation of the slave-boson field (SBMFT),[53,54] only valid for describing spin fluctuations in the Kondo regime, correctly generates the low-energy scale T_K and leads to a local Fermi-liquid behavior at zero temperature (Fig. 1). The SBMFT, however, does suffer from two drawbacks: (a) it leads always to a local Fermi-liquid behavior, even for multichannel models; (b) The SBMFT has a phase transition (originating from the breakdown of the local gauge symmetry of the problem) that separates the low-temperature state from the high-temperature local-moment regime. This latter problem may be corrected by including $1/N$ fluctuations around the mean-field solution.[55] The generalization of the SBMFT to the present problem, two coupled quantum dots in a nonequilibrium situation has been studied in Ref. 47.

(ii) The NCA (Refs. 49 and 50) is the lowest-order self-consistent, fully conserving, and Φ derivable theory in the Baym sense.[56] It is well known that the NCA fails in describing the low-energy Fermi-liquid regime. Neglect of vertex corrections prevents us from a proper description of low-energy excitations. Nevertheless, the NCA has proven to give reliable results for temperatures down to a fraction of T_K.[57] The NCA gives better results in multichannel cases, where the correct non-Fermi-liquid behavior is obtained.[58] Nonetheless, Kroha *et al.*[59] have shown in a series of papers that it is possible to develop systematic corrections to the NCA’s Φ functional that cures the low-temperature pathologies of the NCA. These systematic corrections (the so-called ‘‘conserving T-matrix approximation’’) are able to describe the Fermi-liquid and non-Fermi-liquid regimes on the same footing. It is also possible to formulate the NCA equations for finite[60] U by introducing an extra slave-boson describing double occupancy. The correct Kondo scale is obtained by symmetrizing the NCA diagrams with respect to empty and doubly occupied local states.[61]

The generalization of the NCA to time-dependent phenomena was developed by Langreth and co-workers in a series of papers[62,63] (see also Ref. 64) and later applied to nonequilibrium transport through quantum dots,[12,14,65–67] tunnel junctions and point contacts,[68] nonequilibrium dynamics at surfaces and STM studies.[69–71] Also, this technique has recently been applied to the study of nonequilibrium dynamics in quantum dots in the Kondo regime[72] and to the study of nonequilibrium-induced decoherence[73] also in quantum dots in the Kondo regime. In this work, the NCA is generalized to cope with the present problem, namely, two Anderson impurities, coupled to each other by a tunneling barrier, which are in a nonequilibrium situation.

The paper is divided as follows: In Sec. II, we formulate the Hamiltonian (the general form and its slave-boson formulation) which describes the problem. In Sec. III, we briefly review the nonequilibrium Green’s-function technique, real time Dyson equations for the retarded and lesser Green’s functions, which we use in order to formulate the problem in its fully nonequilibrium form. In Sec. IV, we present our generalization of the NCA technique to the problem. In Sec. IV A, the self-energies obtained within our scheme are presented and discussed. In Sec. IV B, we derive the physical two-particle correlation functions within the NCA approach. In Sec. IV C, we present the fermion and boson self-energies after the projection onto the restricted Hilbert space. We present and discuss in Sec. V various model calculations for the DOS, both in equilibrium and nonequilibrium situations, linear conductance, nonlinear current, and nonlinear differential conductance. We give a series of predictions for the current and finite voltage differential conductance which are relevant for experiments. It is demonstrated that the measurements of the differential conductance $\mathcal{G}=dI/dV$, for the appropriate values of voltages and interdot tunneling couplings, can give a direct observation of the coherent superposition between the many-body Kondo states of each dot. We also give predictions for the temperature dependence of the linear conductance and for the nonlinear differential conductance in the high-voltage regime, where negative differential conductance is obtained for low temperatures.

We include three appendices: In Appendix A, we briefly describe how to obtain the self-energies used in the main text from a Baym functional Φ at lowest order (NCA). In Appendix B, we analyze the equation of motion of the contour-ordered Green's functions, with special emphasis on their off-diagonal components. We prove explicitly that these off-diagonal components vanish for zero interdot tunneling, which allows us to neglect them in the NCA equations for the self-energies as stated in Sec. IV. In Appendix C, we describe the projection procedure used to deal with the constraint in the Hilbert space.

II. MODEL

A. General formulation

As we mentioned already, the double quantum dot can be modeled as a two-impurity Anderson Hamiltonian with an extra term accounting for interimpurity hopping. Each impurity is connected to a different Fermi sea with chemical potential $\mu_L=eV/2$ and $\mu_R=-eV/2$, respectively ($\epsilon_F=0$).

$$H=\sum_{k_{\alpha\in\{L,R\}},\sigma}\epsilon_{k_\alpha}c^{\dagger}_{k_\alpha,\sigma}c_{k_\alpha,\sigma}+\sum_{\alpha\in\{L,R\},\sigma}\epsilon_{\alpha\sigma}d^{\dagger}_{\alpha\sigma}d_{\alpha\sigma}$$
$$+V_0\sum_{k_{\alpha\in\{L,R\}},\sigma}(c^{\dagger}_{k_\alpha,\sigma}d_{\alpha\sigma}+d^{\dagger}_{\alpha\sigma}c_{k_\alpha,\sigma})+V_C\sum_{\sigma}(d^{\dagger}_{L\sigma}d_{R\sigma}$$
$$+d^{\dagger}_{R\sigma}d_{L\sigma})+U_Ln_{L,\uparrow}n_{L,\downarrow}+U_Rn_{R,\uparrow}n_{R,\downarrow}. \qquad (1)$$

The first two terms in the Hamiltonian represent the electrons in the leads and in the dots, respectively. In these Hamiltonians, $c^{\dagger}_{k_{L/R},\sigma}$ ($c_{k_{L/R},\sigma}$) creates (annihilates) an electron with momentum $k_{L/R}$ and spin σ in the left/right lead, and $d^{\dagger}_{L/R\sigma}$ ($d_{L/R\sigma}$) creates (annihilates) an electron with spin σ in the left/right dot. $\epsilon_{k_{L/R}}=\epsilon_k+\mu_{L/R}=\epsilon_k\pm eV/2$ and $\epsilon_{\alpha\sigma}$ are the energies in the leads and the dots, respectively. The third term describes the coupling between each dot and its corresponding lead, and determines the coupling strength $\Delta_{L,R}(\epsilon)=\pi V_0^2\Sigma_{k_{\alpha\in\{L,R\}}}\delta(\epsilon-\epsilon_{k_\alpha})$ (we neglect the k dependency of the tunneling matrix element for simplicity). Each lead is described by a parabolic density of states (bandwidth $W=2D$) centered at the chemical potential, such that we can define the function

$$\Delta_\alpha(\epsilon)=\pi V_0^2\sum_{k_\alpha}\delta(\epsilon-\epsilon_{k_\alpha})$$
$$=\begin{cases}\Delta_0\left[1-\left(\dfrac{\epsilon-\mu_\alpha}{D}\right)^2\right] & \text{if } -D\leqslant\epsilon-\mu_\alpha\leqslant D\\ 0 & \text{otherwise.}\end{cases}$$

The fourth term describes the interdot tunneling. In the absence of the interdot tunneling, this Hamiltonian describes two independent Anderson impurities each of them coupled to different Fermi seas (typically at different chemical potentials). Note that the role of the interdot term is twofold: first, it generates quantum coherence between the impurities; second, it establishes a nonequilibrium situation, that is, when the chemical potentials are different there is a bias voltage across the system and, then, there is an electrical current flowing through the double-dot system. The last terms describe the on-site electron-electron interaction on each dot where $n_{L/R,\sigma}=d^{\dagger}_{L/R\sigma}d_{L/R\sigma}$ are the number operators for spin σ on each dot. The on-site interaction parameters are $U_L=e^2/2C_L$ and $U_R=e^2/2C_R$, where $C_{L/R}$ are the dot capacitances. The neglect of an interdot electron-electron interaction ($\sim U_{\text{interdot}}n_Ln_R$) with $U_{\text{interdot}}\sim C_{LR}/C_LC_R$ corresponds to the experimentally accessible limit of small interdot capacitance (C_{LR}) as compared with the capacitances of each QD to the gates, and implies a vanishing interdot coupling from this source.[74] Experimentally, these parameters governing the Hamiltonian: tunneling couplings, on-site interactions, etc., can be purposefully modified by external gate voltages,[6] which allows to study a variety of rich physical phenomena (spin- and charge-fluctuation regime, nonequilibrium phenomena, etc.) on the same sample.[1–5]

B. Slave-particle representation

We assume $U_L=U_R=U\rightarrow\infty$, forbidding double occupancy on each dot. This is a good approximation for ultrasmall quantum dots in which the on-site interaction is much larger than the coupling strength $\Delta_{L,R}$ (typically more than one order of magnitude).

In the limit $U\rightarrow\infty$, the antiferromagnetic coupling due to superexchange $J\sim t_C^2/U$ vanishes in the model. Nevertheless, we expect our conclusions (for $J=0$) to remain valid for $J\neq0$ in the following limits: (i) small interdot coupling $t_C<\Gamma=2\Delta_0$, provided that $T_K\gg2J$; (ii) large interdot coupling $t_C>\Gamma$, the antiferromagnetic coupling becomes irrelevant. The previous estimations for the limits of validity of our calculation are based on a SBMFT analysis,[41,48] which we expect to remain valid (at least qualitatively) in the presence of fluctuations.

In the limit of $U_L,U_R\rightarrow\infty$ (i.e., $C_L,C_R\rightarrow0$) we can write the Hamiltonian (1) in terms of auxiliary pseudofermions and slave-boson operators plus constraints:

$$H=\sum_{k_{\alpha\in\{L,R\}},\sigma}\epsilon_{k_\alpha}c^{\dagger}_{k_\alpha,\sigma}c_{k_\alpha,\sigma}+\sum_{\alpha\in\{L,R\},\sigma}\epsilon_{\alpha\sigma}f^{\dagger}_{\alpha\sigma}f_{\alpha\sigma}$$
$$+\frac{t_C}{N}\sum_{\sigma}(f^{\dagger}_{L\sigma}b_Lb^{\dagger}_Rf_{R\sigma}+f^{\dagger}_{R\sigma}b_Rb^{\dagger}_Lf_{L\sigma})$$
$$+\frac{V}{\sqrt{N}}\sum_{k_{\alpha\in\{L,R\}},\sigma}(c^{\dagger}_{k_\alpha,\sigma}b^{\dagger}_{\alpha}f_{\alpha\sigma}+f^{\dagger}_{\alpha\sigma}b_{\alpha}c_{k_\alpha,\sigma}). \qquad (2)$$

In the slave-boson representation, the annihilation operator for electrons in the QD's, $d_{\alpha\sigma}$, is decomposed into the SB operator $b^{\dagger}_{\alpha}$ which creates an empty state and a pseudofer-

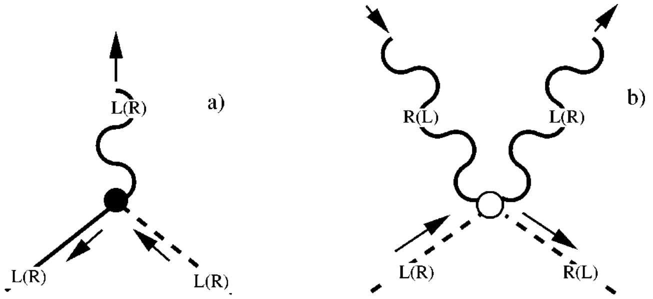

FIG. 2. Interaction vertices. Solid, dashed, and wavy lines represent lead electron, pseudofermion, and slave-boson lines, respectively. Each line carries a left (right) index. (a) Lead-dot hopping vertex $V/\sqrt{N}$ (full circle). Tunneling of an electron from the left (right) dot to the left (right) lead is represented as the decay of the left (right) pseudofermion into a left (right) slave boson and left (right) lead electron. (b) Dot-dot hopping vertex t_C/N (open circle). Tunneling of an electron from the left (right) dot to the right (left) dot is represented as the combination of the left (right) pseudofermion with the right (left) slave boson to decay into a left (right) slave boson and right (left) pseudofermion. Note that this vertex exchanges left and right indices.

mion operator $f_{\alpha\sigma}$ which annihilates the singly occupied state with spin σ in the dot α: $d_{\alpha\sigma}\to b_\alpha^\dagger f_{\alpha\sigma}$ ($d_{\alpha\sigma}^\dagger\to f_{\alpha\sigma}^\dagger b_\alpha$). Note that we have scaled the hopping parameters $V_0=V/\sqrt{N}$ and $V_C=t_C/N$, N being the degeneracy of the level on each dot. The leads are described now by the function

$$\Gamma_\alpha(\epsilon)=N\Delta_\alpha(\epsilon)$$
$$=\pi V^2\sum_{k_\alpha}\delta(\epsilon-\epsilon_{k_\alpha})$$
$$=\begin{cases}\Gamma\left[1-\left(\dfrac{\epsilon-\mu_\alpha}{D}\right)^2\right] & \text{if } -D\leq\epsilon-\mu_\alpha\leq D\\ 0 & \text{otherwise.}\end{cases}$$

This scaling is done in such a way that the parameters $\Gamma=N\Delta_0$ and $\Delta_0/V_C=N\Delta_0/t_C=\Gamma/t_C$ appearing in the expression of the Kondo temperature (see Sec. V and Refs. 41 and 42) have a well-defined $N\to\infty$ limit, namely, there is a well-defined $1/N$ expansion of the physical quantities.

Finally, the physical constraint is that we must work in a subspace of the Hilbert space where the number of auxiliary particles (on each dot) is 1, namely,

$$\hat{Q}_L=\sum_\sigma f_{L\sigma}^\dagger f_{L\sigma}+b_L^\dagger b_L=1,$$
$$\hat{Q}_R=\sum_\sigma f_{R\sigma}^\dagger f_{R\sigma}+b_R^\dagger b_R=1. \tag{3}$$

As we mentioned before, these two constraints come from the physical condition that each dot has to be in one of the three states $|0\rangle$, $|\uparrow\rangle$, or $|\downarrow\rangle$. To simplify the notation we consider henceforth that $\epsilon_{L\sigma}=\epsilon_{R\sigma}=\epsilon_0$. The Hamiltonian (2) has two different kinds of fermion-boson interactions which are given by the vertices in Fig. 2.

III. GREEN'S FUNCTIONS AND SELF-ENERGIES

At this point, we have reduced the original problem described by the Hamiltonian in Eq. (1) to a problem of fermions and bosons interacting through the vertices of Fig. 2 and subject to the constraints in Eq. (3). Properties of the physical electrons can be built up from the Green's functions of the pseudofermions and slave bosons (see Sec. IV B). These Green's functions for the auxiliary fermions and bosons constitute the basic building blocks of the theory. Furthermore, our aim is to study the out-of-equilibrium properties of the system; we need, then, a fully nonequilibrium description of the dynamics of the Green's functions of these auxiliary particles. The appropriate starting point is to derive equations of motion for the time-ordered double-time Green's function of the auxiliary fermion (G) and boson (B) fields on a complex contour. A rigorous and well established way to derive these equations of motion was first introduced by Kadanoff and Baym,[75] and has been related to other nonequilibrium methods (such as the Keldysh method) by Langreth, see Ref. 76 for a review.

The time-ordered double-time Green's function are defined as (subindices are omitted here).

$$iG(t,t')\equiv\langle T_c f(t)f^\dagger(t')\rangle,$$
$$iB(t,t')\equiv\langle T_c b(t)b^\dagger(t')\rangle, \tag{4}$$

or in terms of their analytic pieces,

$$iG(t,t')=G^>(t,t')\,\theta(t-t')-G^<(t,t')\,\theta(t'-t),$$
$$iB(t,t')=B^>(t,t')\,\theta(t-t')+B^<(t,t')\,\theta(t'-t). \tag{5}$$

The time-ordering operator T_c and the step functions θ operate along a contour c in the complex plane. It will not matter in the derivation given here whether c is taken to be the Keldysh contour, the Kadanoff-Baym contour, or a more general choice. $G^<(t,t')\equiv\langle f^\dagger(t')f(t)\rangle$ and $B^<(t,t')\equiv\langle b^\dagger(t')b(t)\rangle$ are the so-called lesser Green's functions, and $G^>(t,t')\equiv\langle f(t)f^\dagger(t')\rangle$ and $B^>(t,t')\equiv\langle b(t)b^\dagger(t')\rangle$ are the greater ones.

The retarded Green's functions can be written in terms of these analytic pieces as

$$iG^r(t,t')=[G^>(t,t')+G^<(t,t')]\theta(t-t'),$$
$$iB^r(t,t')=[B^>(t,t')-B^<(t,t')]\theta(t-t'). \tag{6}$$

The advanced ones can be obtained from $G^r(t,t')=[G^a(t',t)]^*$.

The basic starting equations follow directly from the Dyson equations in complex time space:

$$\left(i\frac{\partial}{\partial t}-\epsilon_0\right)G(t,t')=\delta(t-t')+\int_c dt_1\Sigma(t,t_1)G(t_1,t'),$$
$$i\frac{\partial}{\partial t}B(t,t')=\delta(t-t')+\int_c dt_1\Pi(t,t_1)B(t_1,t'). \tag{7}$$

Applying analytic continuation rules[76] we can write Dyson equations in real time space, which relate the lesser and the greater Green's functions with the retarded and advanced ones:

$$\left(i\frac{\partial}{\partial t}-\epsilon_0\right)G^{\gtrless}(t,t')=\int_{-\infty}^{\infty}dt_1[\Sigma^r(t,t_1)G^{\gtrless}(t_1,t')+\Sigma^{\gtrless}(t,t_1)G^a(t_1,t')],$$

$$i\frac{\partial}{\partial t}B^{\gtrless}(t,t')=\int_{-\infty}^{\infty}dt_1[\Pi^r(t,t_1)B^{\gtrless}(t_1,t')+\Pi^{\gtrless}(t,t_1)B^a(t_1,t')]. \tag{8}$$

The retarded (and advanced) Green's functions follow usual Dyson equations:

$$\left(i\frac{\partial}{\partial t}-\epsilon_0\right)G^r(t,t')=\delta(t-t')+\int_{-\infty}^{\infty}dt_1\Sigma^r(t,t_1)G^r(t_1,t'),$$

$$i\frac{\partial}{\partial t}B^r(t,t')=\delta(t-t')+\int_{-\infty}^{\infty}dt_1\Pi^r(t,t_1)B^r(t_1,t'). \tag{9}$$

The set of Dyson equations is closed by choosing a suitable approximation for the self-energies Σ and Π, and hence for their analytic pieces $\Sigma^<$, $\Sigma^>$, $\Pi^<$, and $\Pi^>$. We describe in the following section the noncrossing approximation used to solve our problem.

IV. NONCROSSING APPROXIMATION

A. Self-energies

We use the NCA technique[49,50] for obtaining the self-energies $\Sigma_{L(R),\sigma}(t,t')$, $\Pi_{L(R)}(t,t')$ in Eq. (7) and their real time analytic continuations. Hereafter, since we focus on static nonequilibrium, dc voltages, the time-translational invariance is thus not broken, i.e., all quantities depend only on the time difference $t-t'$.[77,78] Nonetheless, our NCA equations for the self-energies, see Eqs. (10) and (11) below, together with Dyson equations in real time, Eqs. (8) and (9), are valid for general situations with broken time-translational symmetry by just substituting $(t-t')\rightarrow(t,t')$ and solving the fully time-dependent problem.

As we already mentioned, the NCA technique can be justified as an $1/N$ expansion, at lowest order in perturbation theory, although it is better regarded as a fully conserving, self-consistent, and Φ derivable theory in the Baym sense.[56] The exact Φ is defined as the set of diagrams consisting of all vacuum skeleton diagrams built out of fully renormalized Green's functions and the bare vertex, weighted so that each self-energy is the functional derivative of Φ with respect to the corresponding skeleton propagator. It was shown by Baym that this requirement is sufficient to guarantee that the propagator equations so obtained exactly satisfy all the conservation laws of the problem, and that the predictions for a physical quantity are independent (to all orders) of which of the several available (exact) expressions for that quantity is used to evaluate it. Approximations that are not Φ derivable generally do not satisfy either of the above requirements.

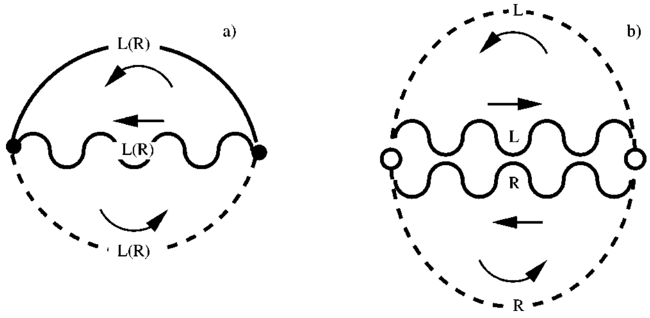

FIG. 3. Diagrammatic representation of the generating functional $\Phi^{NCA}=\Phi_1+\Phi_2$ of our NCA approximation. Solid, dashed, and wavy lines represent lead electron, pseudofermion, and slave-boson lines, respectively. Each line carries a left (right) index. Full circle, lead-dot hopping vertex $V/\sqrt{N}$; open circle, dot-dot hopping vertex t_C/N. The self-energies are obtained by taking the functional derivative of Φ^{NCA} with respect to the corresponding Green's function. (a) Lead-dot functional Φ_1 [leading order $O(1)$]. (b) Dot-dot functional Φ_2 [leading order $O(1/N)$].

To lowest order in both vertices (NCA), we obtain the Baym functional of Fig. 3. This functional consists of two terms $\Phi^{NCA}=\Phi_1+\Phi_2$. To lowest order in the lead-dot vertex we obtain the functional Φ_1 [Fig. 3(a)] which is of leading order $O(1)$ [the order $O(1/N)$ for the vertex $V/\sqrt{N}$ is not skeleton]. The functional Φ_2 [Fig. 3(b)] is constructed from the dot-dot vertex and is of leading order $O(1/N)$. The NCA solution obtained from $\Phi^{NCA}=\Phi_1+\Phi_2$ is expressed diagrammatically in Figs. 4 and 5. These self-energies are obtained by the functional derivation of the Baym functional (Fig. 3) $\Sigma=\partial\Phi^{NCA}/\partial G$ and $\Pi=\partial\Phi^{NCA}/\partial B$ (for details see Appendix A). This guarantees that our approximation is conserving. The obtained self-energies are of leading order $O(1)+O(1/N)$ (bosons) and $O(1/N)+O(1/N^2)$ (fermions).

In principle, it is posible to construct another generating functional from the dot-dot vertex which contains off-diagonal Green's functions. This functional can be constructed from Φ_2 by replacing all the diagonal fermion and boson Green's functions by off-diagonal ones. The corresponding self-energies are equivalent to those of Figs. 4(b) and 5(b) with all the diagonal Green's functions replaced by the off-diagonal ones. However, it can be shown that the bare

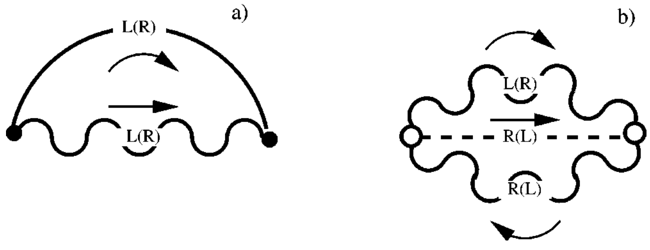

FIG. 4. Fermion self-energy. Solid, dashed, and wavy lines represent lead electron, pseudofermion, and slave-boson lines, respectively. Each line carries a left (right) index. Full circle, lead-dot hopping vertex $V/\sqrt{N}$; open circle, dot-dot hopping vertex t_C/N. The leading order of this self-energy is $O(1/N)+O(1/N^2)$.

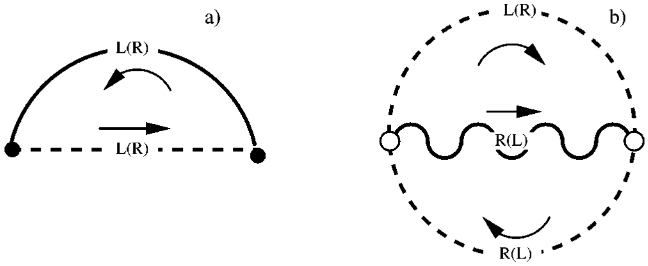

FIG. 5. Boson self-energy. Solid, dashed, and wavy lines represent lead electron, pseudofermion, and slave-boson lines, respectively. Each line carries a left (right) index. Full circle, lead-dot hopping vertex $V/\sqrt{N}$; open circle; dot-dot hopping vertex t_C/N. The leading order of this self-energy is $O(1)+O(1/N)$.

($t_C=0$) off-diagonal Green's functions are zero (see Appendix B), namely, the off-diagonal functional vanishes to order t_C^2, i.e., it does not contribute to leading order with terms $O(1/N)$ in the interdot vertex. In particular, this implies that there are no off-diagonal self-energies to second order in the interdot vertex. It is, thus, consistent to neglect off-diagonal self-energies within the NCA. This way, our NCA guarantees that all diagrams of leading order $O(1/N)$ are included within a more general subset of diagrams which includes terms to all orders in both vertices.

Applying real time analytical continuation[76] to Eq. (A7) in appendix A (see diagram in Fig. 4), we obtain the lesser, greater, and retarded components of the fermion self-energy:

$$\Sigma^{<}_{L(R),\sigma}(t-t')=\frac{1}{N}K^{<}_{L(R),\sigma}(t-t')B^{<}_{L(R)}(t-t')+\left(\frac{t_C}{N}\right)^2 \times G^{<}_{R(L),\sigma}(t-t')B^{>}_{R(L)}(t'-t)B^{<}_{L(R)}(t-t'),$$

$$\Sigma^{>}_{L(R),\sigma}(t-t')=\frac{1}{N}K^{>}_{L(R),\sigma}(t-t')B^{>}_{L(R)}(t-t')+\left(\frac{t_C}{N}\right)^2 \times G^{>}_{R(L),\sigma}(t-t')B^{<}_{R(L)}(t'-t)B^{>}_{L(R)}(t-t'),$$

$$\begin{aligned}\Sigma^{r}_{L(R),\sigma}(t-t')=&\frac{1}{N}\{K^{>}_{L(R),\sigma}(t-t')B^{r}_{L(R)}(t-t')\\&+K^{r}_{L(R),\sigma}(t-t')B^{<}_{L(R)}(t-t')\}+\left(\frac{t_C}{N}\right)^2\\&\times\{G^{>}_{R(L),\sigma}(t-t')B^{<}_{R(L)}(t'-t)B^{r}_{L(R)}(t-t')\\&+G^{>}_{R(L),\sigma}(t-t')B^{a}_{R(L)}(t'-t)B^{<}_{L(R)}(t-t')\\&+G^{r}_{R(L),\sigma}(t-t')B^{>}_{R(L)}(t'-t)B^{<}_{L(R)}(t-t')\},\end{aligned}\tag{10}$$

where the quantities $K_{L(R),\sigma}$ are defined in terms of the fermion propagator in the left (right) lead as $K_{L(R),\sigma}=V^2\Sigma_{k_{L(R)}}g_{k_{L(R)},\sigma}$ (see Sec. IV C). The corresponding expressions for slave-boson self-energies [Eq. (A8) in Appendix A] corresponding to Fig. 5 are

$$\begin{aligned}\Pi^{<}_{L(R)}(t-t')=&\frac{1}{N}\sum_{\sigma}K^{>}_{L(R),\sigma}(t'-t)G^{<}_{L(R),\sigma}(t-t')\\&+\left(\frac{t_C}{N}\right)^2\sum_{\sigma}B^{<}_{R(L)}(t-t')G^{>}_{R(L),\sigma}(t'-t)\\&\times G^{<}_{L(R),\sigma}(t-t'),\end{aligned}$$

$$\begin{aligned}\Pi^{>}_{L(R)}(t-t')=&\frac{1}{N}\sum_{\sigma}K^{<}_{L(R),\sigma}(t'-t)G^{>}_{L(R),\sigma}(t-t')\\&+\left(\frac{t_C}{N}\right)^2\sum_{\sigma}B^{>}_{R(L)}(t-t')G^{<}_{R(L),\sigma}(t'-t)\\&\times G^{>}_{L(R),\sigma}(t-t'),\end{aligned}$$

$$\begin{aligned}\Pi^{r}_{L(R)}(t-t')=&\frac{1}{N}\sum_{\sigma}\{K^{<}_{L(R),\sigma}(t'-t)G^{r}_{L(R),\sigma}(t-t')\\&+K^{a}_{L(R),\sigma}(t'-t)G^{<}_{L(R),\sigma}(t-t')\}\\&+\left(\frac{t_C}{N}\right)^2\sum_{\sigma}\{B^{>}_{R(L)}(t-t')G^{<}_{R(L),\sigma}(t'-t)\\&\times G^{r}_{L(R),\sigma}(t-t')-B^{r}_{R(L)}(t-t')\\&\times G^{<}_{R(L),\sigma}(t'-t)G^{<}_{L(R),\sigma}(t-t')\\&+B^{<}_{R(L)}(t-t')G^{a}_{R(L),\sigma}(t'-t)G^{<}_{L(R),\sigma}(t-t')\}.\end{aligned}\tag{11}$$

Equations (10) and (11) are the unprojected full NCA self-energies coming from the generating functional. The projection of these quantities onto the physical subspace $\hat{Q}_{\alpha\in\{L,R\}}=1$ is discussed in Appendix C.

B. Physical correlation functions

The physical lesser and greater correlation functions ($\alpha\in\{L,R\}$) are

$$A^{<}_{\alpha\sigma}(t-t')\equiv\langle d^{\dagger}_{\alpha\sigma}(t')d_{\alpha\sigma}(t)\rangle,$$

$$A^{>}_{\alpha\sigma}(t-t')\equiv\langle d_{\alpha\sigma}(t)d^{\dagger}_{\alpha\sigma}(t')\rangle.\tag{12}$$

In terms of slave operators, they become the two-particle correlation functions:

$$A^{<}_{\alpha\sigma}(t-t')\equiv\langle f^{\dagger}_{\alpha\sigma}(t')b_{\alpha}(t')b^{\dagger}_{\alpha}(t)f_{\alpha\sigma}(t)\rangle,$$

$$A^{>}_{\alpha\sigma}(t-t')\equiv\langle b^{\dagger}_{\alpha}(t)f_{\alpha\sigma}(t)f^{\dagger}_{\alpha\sigma}(t')b_{\alpha}(t')\rangle.\tag{13}$$

The evaluation of these two-particle correlation functions would require, in principle a further diagrammatic expansion. Within the NCA, however, one neglects vertex corrections[79] and keeps only the lowest-order term in the expansion of the two-particle correlation function (Fig. 6):

$$\begin{aligned}A^{<}_{\alpha\sigma}(t-t')=&\langle f^{\dagger}_{\alpha\sigma}(t')f_{\alpha\sigma}(t)\rangle\langle b_{\alpha}(t')b^{\dagger}_{\alpha}(t)\rangle\\=&G^{<}_{\alpha\sigma}(t-t')B^{>}_{\alpha}(t'-t),\end{aligned}$$

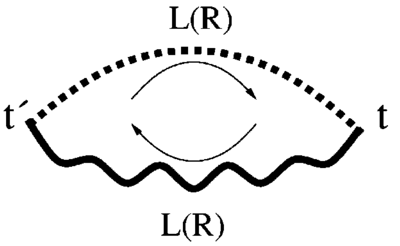

FIG. 6. Diagrammatic representation of the physical two-particle correlation function within the NCA. The neglected vertex corrections are $O(1/N^2)$ (Ref. 53).

$$A^{>}_{\alpha\sigma}(t-t')=\langle b^{\dagger}_{\alpha}(t)b_{\alpha}(t')\rangle\langle f_{\alpha\sigma}(t)f^{\dagger}_{\alpha\sigma}(t')\rangle$$
$$=B^{<}_{\alpha}(t'-t)G^{>}_{\alpha\sigma}(t-t'). \qquad (14)$$

Using the identities

$$G^{>}_{L(R),\sigma}(t-t')=i[G^{r}_{L(R),\sigma}(t-t')-G^{a}_{L(R),\sigma}(t-t')]$$
$$-G^{<}_{L(R),\sigma}(t-t'),$$
$$B^{>}_{L(R),\sigma}(t-t')=i[B^{r}_{L(R),\sigma}(t-t')-B^{a}_{L(R),\sigma}(t-t')]$$
$$+B^{<}_{L(R),\sigma}(t-t'), \qquad (15)$$

Eq. (14) can be rewritten as

$$A^{<}_{\alpha\sigma}(t-t')=G^{<}_{\alpha\sigma}(t-t')\{i[B^{r}_{\alpha,\sigma}(t'-t)-B^{a}_{\alpha,\sigma}(t'-t)]$$
$$+B^{<}_{\alpha,\sigma}(t'-t)\}$$
$$A^{>}_{\alpha\sigma}(t-t')=B^{<}_{\alpha}(t'-t)\{i[G^{r}_{\alpha,\sigma}(t-t')-G^{a}_{\alpha,\sigma}(t-t')]$$
$$-G^{<}_{\alpha,\sigma}(t-t')\}. \qquad (16)$$

Now, according to the projection procedure explained in Appendix C (see also Ref. 62), the terms $G^{<}_{\alpha\sigma}(t-t')B^{<}_{\alpha,\sigma}(t'-t)$ and $B^{<}_{\alpha}(t'-t)G^{<}_{\alpha,\sigma}(t-t')$ have to be projected out [they are of the order of $O(e^{-2i\beta\lambda_{\alpha}})$]. This is accomplished by making

$$G^{>}_{L(R),\sigma}(t-t')=i[G^{r}_{L(R),\sigma}(t-t')-G^{a}_{L(R),\sigma}(t-t')]$$
$$B^{>}_{L(R),\sigma}(t-t')=i[B^{r}_{L(R),\sigma}(t-t')-B^{a}_{L(R),\sigma}(t-t')], \qquad (17)$$

which gives the following physical correlation functions:

$$A^{<}_{\alpha\sigma}(t-t')=iG^{<}_{\alpha\sigma}(t-t')[B^{r}_{\alpha,\sigma}(t'-t)-B^{a}_{\alpha,\sigma}(t'-t)],$$
$$A^{>}_{\alpha\sigma}(t-t')=iB^{<}_{\alpha}(t'-t)[G^{r}_{\alpha,\sigma}(t-t')-G^{a}_{\alpha,\sigma}(t-t')],$$
$$A^{r(a)}_{\alpha\sigma}(t-t')=G^{r(a)}_{\alpha,\sigma}(t-t')B^{<}_{\alpha}(t'-t)$$
$$-G^{<}_{\alpha\sigma}(t-t')B^{a(r)}_{\alpha,\sigma}(t'-t). \qquad (18)$$

These Green's functions have to be calculated with the corresponding projected self-energies, as discussed in the following section.

C. Physical self-energies

The final set of projected self-energies is (see Appendix C for details)

$$\Sigma^{r}_{L(R),\sigma}(\tau)=\left\{\frac{1}{N}\tilde{K}^{>}_{L(R),\sigma}(\tau)+i\left(\frac{t_C}{N}\right)^2[\tilde{G}^{r}_{R(L),\sigma}(\tau)\right.$$
$$\left.-\tilde{G}^{a}_{R(L),\sigma}(\tau)]\frac{\tilde{B}^{<}_{R(L)}(-\tau)}{Z_{R(L)}}\right\}\tilde{B}^{r}_{L(R)}(\tau),$$

$$\Pi^{r}_{L(R)}(\tau)=\left\{\frac{1}{N}\sum_{\sigma}\tilde{K}^{<}_{L(R),\sigma}(-\tau)+i\left(\frac{t_C}{N}\right)^2\sum_{\sigma}[\tilde{B}^{r}_{R(L)}(\tau)\right.$$
$$\left.-\tilde{B}^{a}_{R(L)}(\tau)]\frac{\tilde{G}^{<}_{R(L),\sigma}(-\tau)}{Z_{R(L)}}\right\}\tilde{G}^{r}_{L(R),\sigma}(\tau). \qquad (19)$$

$$\Sigma^{<}_{L(R),\sigma}(\tau)=\left\{\frac{1}{N}\tilde{K}^{<}_{L(R),\sigma}(\tau)+i\left(\frac{t_C}{N}\right)^2\frac{\tilde{G}^{<}_{R(L),\sigma}(\tau)}{Z_{R(L)}}\right.$$
$$\left.\times[\tilde{B}^{r}_{R(L)}(-\tau)-\tilde{B}^{a}_{R(L)}(-\tau)]\right\}\tilde{B}^{<}_{L(R)}(\tau),$$

$$\Pi^{<}_{L(R)}(\tau)=\left\{\frac{1}{N}\sum_{\sigma}\tilde{K}^{>}_{L(R),\sigma}(-\tau)+i\left(\frac{t_C}{N}\right)^2\sum_{\sigma}\frac{\tilde{B}^{<}_{R(L)}(\tau)}{Z_{R(L)}}\right.$$
$$\left.\times[\tilde{G}^{r}_{R(L),\sigma}(-\tau)-\tilde{G}^{a}_{R(L),\sigma}(-\tau)]\right\}\tilde{G}^{<}_{L(R),\sigma}(\tau).$$
$$(20)$$

Where we have introduced the notation $\tau=t-t'$. The NCA equations depend on the conduction electrons through the quantities $\tilde{K}$ which are defined in terms of the Fourier transforms of the *bare* conduction-electron propagators (namely, without dot-lead coupling) as

$$\tilde{K}^{\gtrless}_{\alpha,\sigma}(\epsilon)=V^2\left[-2\,\mathrm{Im}\left\{\sum_{k_\alpha}\frac{1}{\epsilon-\epsilon_{k_\alpha}+i\eta}\right\}f^{\gtrless}_{\alpha}(\epsilon)\right]$$
$$=2\pi V^2\sum_{k_\alpha}\delta(\epsilon-\epsilon_{k_\alpha})f^{\gtrless}_{\alpha}(\epsilon)=2\Gamma_{\alpha}(\epsilon)f^{\gtrless}_{\alpha}(\epsilon),$$

where $f^{<}_{\alpha}(\epsilon)=1/(e^{\beta(\epsilon-\mu_\alpha)}+1)$ is the Fermi function and $f^{>}_{\alpha}(\epsilon)=1-f^{<}_{\alpha}(\epsilon)$ (see Ref. 62).

The Green's functions $\tilde{G}$ and $\tilde{B}$, which are full propagators with respect to the lead-dot hopping, *do not* include the interdot coupling. The factors Z_L and Z_R can be identified with the left and right charges in the absence of the interdot hopping. They can be obtained from the left and right charges of two independent single-impurity problems (at different chemical potentials μ_L and μ_R, respectively), namely,

$$Z_{\alpha}=\int\frac{d\omega}{2\pi}[N\tilde{G}^{<}_{\alpha}(\omega)+\tilde{B}^{<}_{\alpha}(\omega)].$$

It is important to emphasize two aspects of the projection: (i) the simplification of the propagators ($K\rightarrow\widetilde{K}$, $G\rightarrow\widetilde{G}$, and $B\rightarrow\widetilde{B}$) is *required* by the projection procedure (see Appendix C) and is not an additional approximation; (ii) this should not be construed to imply that there is no interdot correction in the slave-particle Green's functions that enter into the physical correlation functions of Eq. (18).

Finally, we note that the structure of the self-energies allows for a very intuitive physical interpretation: each left (right) self-energy has the structure

$$\{\mathrm{Kernel}^{(1)}+\mathrm{Kernel}^{(2)}\}\times\mathrm{propagator}.$$

$\mathrm{Kernel}^{(1)}$ contains the addition or substraction spectrum of conduction electrons in the left (right) lead, i.e., $\widetilde{K}^{\gtrless}_{\alpha,\sigma}$. $\mathrm{Kernel}^{(2)}$ contains the addition or substraction spectrum of *physical* electrons in the right (left) dot. This can be shown by comparing the second term of each self-energy with the expressions for the physical correlation functions in Eq. (18), which allows us to rewrite Eqs. (19) and (20) as

$$\Sigma^{r}_{L(R),\sigma}(\tau)=\left\{\frac{1}{N}\widetilde{K}^{>}_{L(R),\sigma}(\tau)+i\left(\frac{t_C}{N}\right)^2\frac{\widetilde{A}^{>}_{R(L),\sigma}(\tau)}{Z_{R(L)}}\right\}\widetilde{B}^{r}_{L(R)}(\tau),$$

$$\Pi^{r}_{L(R)}(\tau)=\left\{\frac{1}{N}\sum_{\sigma}\widetilde{K}^{<}_{L(R),\sigma}(-\tau)+i\left(\frac{t_C}{N}\right)^2\sum_{\sigma}\frac{\widetilde{A}^{<}_{R(L),\sigma}(-\tau)}{Z_{R(L)}}\right\}\widetilde{G}^{r}_{L(R),\sigma}(\tau). \tag{21}$$

$$\Sigma^{<}_{L(R),\sigma}(\tau)=\left\{\frac{1}{N}\widetilde{K}^{<}_{L(R),\sigma}(\tau)+i\left(\frac{t_C}{N}\right)^2\frac{\widetilde{A}^{<}_{R(L),\sigma}(\tau)}{Z_{R(L)}}\right\}\widetilde{B}^{<}_{L(R)}(\tau),$$

$$\Pi^{<}_{L(R)}(\tau)=\left\{\frac{1}{N}\sum_{\sigma}\widetilde{K}^{>}_{L(R),\sigma}(-\tau)+i\left(\frac{t_C}{N}\right)^2\sum_{\sigma}\frac{\widetilde{A}^{>}_{R(L),\sigma}(-\tau)}{Z_{R(L)}}\right\}\widetilde{G}^{<}_{L(R),\sigma}(\tau). \tag{22}$$

Equation (21) and (22) show explicitly that the interdot term is renormalized by correlations [the interdot coupling terms of the left (right) self-energies depend on the right (left) dot spectra through $\widetilde{A}^{<}_{R(L)\sigma}$ or $\widetilde{A}^{>}_{R(L)\sigma}$ in $\mathrm{Kernel}^{(2)}$]. Other examples where the structure of the kernels in the NCA self-energies affects the Kondo physics are, for instance, the Kondo effect in metal grains[80] or the Kondo effect in normal-superconducting systems.[81] Equations (21) and (22) constitute the main result of this section. The projected self-energies inserted in the appropriate Dyson equation give an overall result in Eq. (18) for the physical correlation functions, which has the correct order. Of course, in the absence of the interdot coupling we recover from Equations (21) and (22) two independent sets of NCA equations for the left and right single-impurity problems. These equations are in agreement with the ones previously obtained in Refs. 14, 62, and 68.

The equations for the self-energies, together with the Dyson equations for the retarded and lesser Green's functions and the normalization conditions, close the set of equations to be solved. We numerically iterate them to convergence.

V. RESULTS

A. Density of states

Here we present results for the left and right dot densities of states, both for equilibrium and finite voltage ($\mu_L=V/2$, $\mu_R=-V/2$) situations. We use the following parameters in the calculations (unless otherwise stated): $\epsilon_0=-2.5$, $T=0.003$, and $D=6$ (all energies are given in units of Γ). The Kondo temperature corresponding to these parameters is $T_K^0\sim 3.7\times 10^{-4}$ (here, the superscript "0" means without the interdot coupling, namely, the Kondo temperature of the single-impurity problem corresponding to these parameters), as calculated from the Bethe ansatz analytical solution ($N=2$):[7,50]

$$T_K^0=\Gamma(1+1/2)D_r(\Gamma/\pi D_r)^{1/2}\exp(-\pi|\epsilon_0|/\Gamma). \tag{23}$$

$\Gamma(x)$ is the gamma function and the rescaling $D_r=\exp(-1/2)D$ accounts for the assumed parabolic DOS's in the leads instead of the rectangular one used in the Bethe ansatz solution.[62] Note, finally, that in order to compare with the SBMFT results,

$$T_K^{SBMFT}\sim D_r\exp(-\pi|\epsilon_0|/\Gamma)\sim 4T_K^0.$$

It is known from the SBMFT (Refs. 41, 42, and 47) and from numerical renormalization-group[43] calculations that the effective Kondo temperature T_K^{DD} of the double-dot system grows exponentially with the interdot hopping,

$$T_K^{DD}\sim T_K^{SBMFT}\exp\left[\frac{t_C}{\Gamma}\arctan\left(\frac{t_C}{\Gamma}\right)\right].$$

It is not possible to extract an analytical expression for the Kondo temperature from our set of coupled NCA equations, and so no possibility to check the previous expression *a priori*; nevertheless, we choose relatively high temperatures $T>T_K^0$ in all our calculations in order to prevent the expected low-temperature pathologies should the effective Kondo temperature T_K^{DD} increase exponentially with the interdot hopping as predicted by the SBMFT and the numerical renormalization-group techniques.

In Fig. 7, the QD DOS at equilibrium (here, of course, the left and right dots are equivalent) is plotted for increasing values of the interdot tunneling. The full DOS [Fig. 7(a)] shows the splitting of the main peak (energy scale for charge fluctuations) originating from the interdot coupling which generates quantum coherence between the dots. The splitting in the DOS corresponds to the formation of bonding and antibonding combinations of the single-particle levels, i.e., $\epsilon_{\pm}=\epsilon_0\mp t_C$ due to the interdot tunneling. Figure 7(b) shows

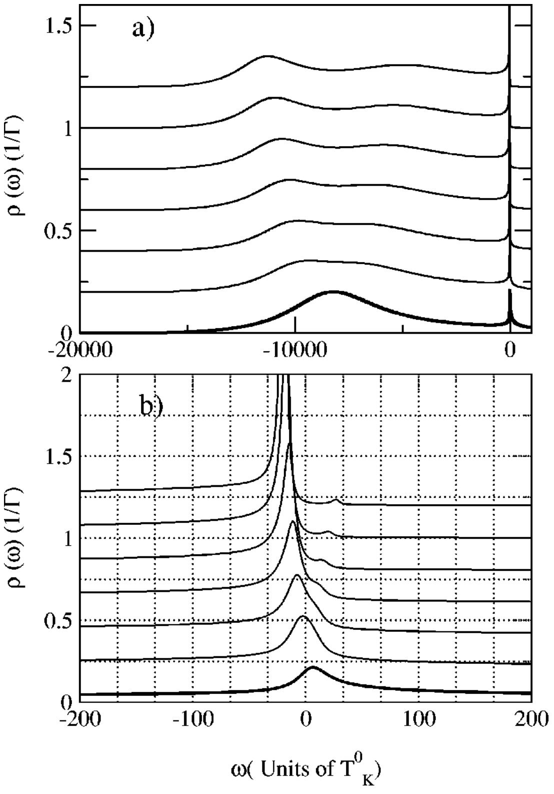

FIG. 7. Equilibrium density of states (DOS) for different values of the interdot hopping $t_C=0.0$, 1.0, 1.2, 1.4, 1.6, 1.8, and 2.0 (units of Γ). The curves are shifted vertically for clarity. $T_K^0=0.000\,37\Gamma$. (a) Full DOS. The splitting in the DOS corresponds to the formation of bonding and antibonding combinations of the single-particle levels due to interdot tunneling. (b) Blowup of the low-frequency region around the Kondo peak. As the interdot coupling increases, the Kondo peak also splits. Importantly, this splitting, which is a manifestation of quantum coherence between the two many-body Kondo states on each dot, is much smaller than the splitting of the broad peak, see main text.

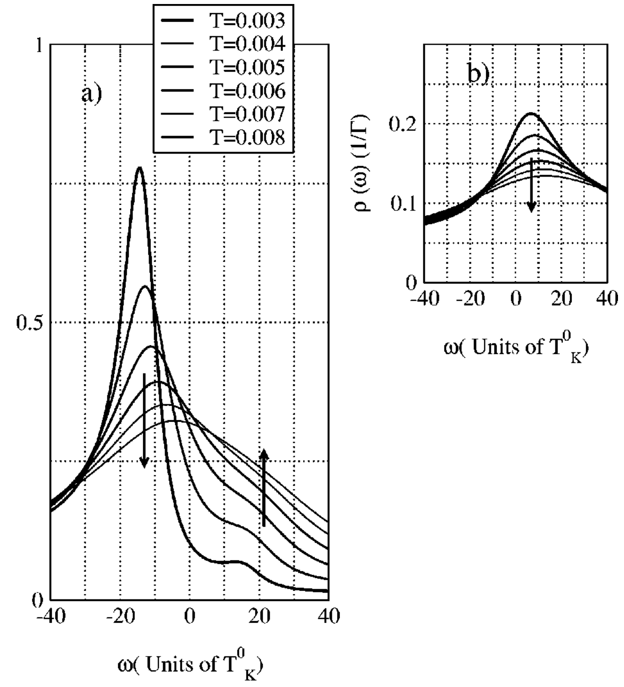

FIG. 8. Temperature dependence of the equilibrium density of states (DOS) around the Fermi level. The arrows indicate the direction of increasing temperatures. $T_K^0=0.000\,37\Gamma$. (a) DOS of the coupled dot problem for $t_C=1.6\Gamma$. The structure originating from the interdot coupling is still visible at temperatures $T\gtrsim 10T_K^0$. (b) Reduction of the Kondo peak for the single-impurity problem as the temperature increases. At the highest studied temperature $T\sim 20T_K^0$ the Kondo peak is almost suppressed as compared with the coupled dot system.

a blowup of the low-frequency part of the DOS around the Fermi level. As we increase the interdot coupling, the Kondo peak also splits into the bonding and antibonding combinations. Importantly, the energy scale for this splitting of the Kondo peak, which is a manifestation of quantum coherence between the two many-body Kondo states on each dot, is much smaller than the one corresponding to the splitting of the broad peak (which is a manifestation of coherence between single-particle states). We have, then, $\Delta\tilde{\epsilon}=2\tilde{t}_C\ll\Delta\epsilon=2t_C$, where $\Delta\tilde{\epsilon}$ and $\Delta\epsilon=2t_C$ are the splitting of the Kondo peak and the single-particle splitting, respectively. This reduction of the splitting, namely, $\tilde{t}_C\ll t_C$, is caused by the strong Coulomb repulsion on each dot (see Sec. IV C). Typical values of this splitting are in the range $\sim 10T_K^0$–$40T_K^0$ (note that the single-particle splittings are in the range $\sim 10^3T_K^0-10^4T_K^0$). These obtained values for the reduced splitting of the Kondo resonance are in good semiquantitative agreement with the mean-field slave-boson calculation.[40–42,47]

The behavior at different temperatures is studied in Fig. 8 where we plot the DOS of the coupled dot problem [Fig. 8(a)] for $t_C=1.6$ at different temperatures. The splitting originating from the interdot coupling is still visible at temperatures $T\gtrsim 10T_K^0$. For comparison, we show in Fig. 8(b) the reduction of the Kondo peak for the single-impurity problem as the temperature increases. At the highest studied temperature $T\sim 20T_K^0$ the Kondo peak for the single-impurity system is almost suppressed as compared with the coupled dot system. This is in good qualitative agreement with the previous statement that $T_K^{DD}>T_K^0$.[41–43,47] It is worth noting that the splitting of the Kondo resonance is robust at temperatures higher than T_K^0; experimentally this is of the most relevance: according to this result, the experimental conditions for studying Kondo physics in coupled QD's are less demanding than in single QD's (temperatures much lower than T_K^0 are needed in order to observe Kondo-related features in the transport properties of single[1–5] QD's).

B. Nonlinear transport properties

We have proven in the preceding section that the interdot coupling generates quantum coherence between the dots. This quantum coherence is reflected in the DOS of each QD as a splitting, *both in the charge-fluctuation and spin-fluctuation parts of the spectrum*. We are interested in Kondo physics and the obvious question we want to answer is thus: Can we observe the splitting of the Kondo peak, induced by

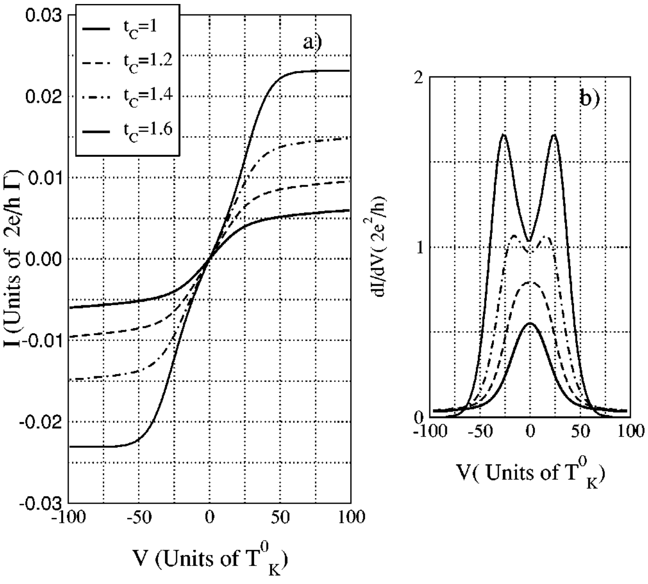

FIG. 9. Nonlinear transport properties of the DQD system for different interdot couplings (in units of Γ) for $T=0.003\approx 8T_K^0$ with $T_K^0=0.000\,37\Gamma$. (a) Current-voltage characteristics. (b) Differential conductance at finite voltage. The zero-bias anomaly first broadens and then splits with increasing interdot hopping. The splitting of the zero-bias anomaly reflects quantum coherence between the two many-body Kondo states on each QD.

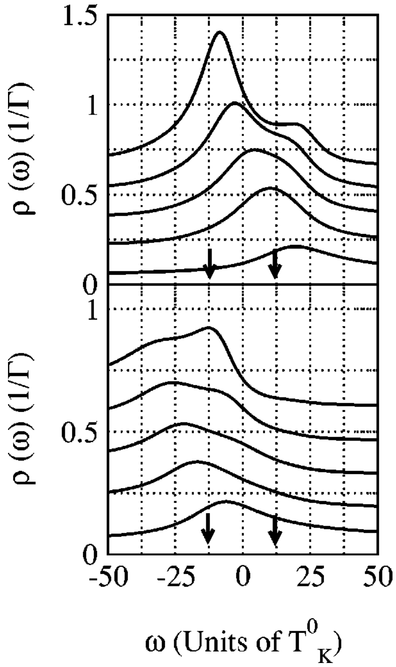

FIG. 10. Nonequilibrium DOS ($\mu_L=V/2=12.5T_K^0, \mu_R=-V/2=-12.5T_K^0$) for different values of the interdot hopping, $t_C=0.0$, 1.0, 1.2, 1.4, and 1.6 (units of Γ). The curves are shifted vertically for clarity. $T_K^0=0.000\,37\Gamma$. Top: left DOS. Bottom: right DOS. The arrows mark the position of the chemical potentials.

the interdot coupling, in a differential conductance measurement? The answer to the previous question is nontrivial because we are dealing with the nonequilibrium physics of strongly correlated electrons and hence the spectral functions are expected to strongly depend on the applied bias voltage (shift and broadening of the peaks). In other words, the differential conductance curve does not just mimic the zero-voltage DOS (as it does for noninteracting electrons). From the experimental point of view this is a timely and crucial question: the observation of such a splitting would prove the remarkable phenomenon of quantum coherence between *the two Kondo many-body states on each dot.* Experiments by Oosterkamp *et al.*[36] and Blick *et al.*[38] have proven quantum coherence between single-particle states in coupled QD's. Also, some signatures of coherence between Kondo states in a double quantum dot system have been reported recently by Jeong *et al.* in Ref. 39. The first step in order to answer our question is to calculate the current through the double-dot system. We follow the standard nonequilibrium approach to transport through a region of interacting electrons[11,82] and relate the current through each dot to its retarded and lesser Green's functions:

$$I_{\alpha\in\{L,R\}}=-\frac{2e}{h}\int d\epsilon\Gamma_{\alpha}(\epsilon)[2\mathrm{Im}\;A^{r}_{\alpha}(\epsilon)f_{\alpha}(\epsilon)+A^{<}_{\alpha}(\epsilon)]. \tag{24}$$

Here, $A^r_\alpha(\epsilon)$ and $A^<_\alpha(\epsilon)$ are the Fourier transforms of the retarded and lesser physical Green's functions of Eq. (18).

The total current through the system is calculated as $I=(I_L-I_R)/2$. The differential conductance $\mathcal{G}=dI/dV$ is calculated by the numerical differentiation of the current-voltage (I-V) curves.

We study in Fig. 9 the nonlinear transport properties of the DQD system. We plot in Fig. 9(a) the I-V characteristics for different values of the interdot hopping. As the interdot hopping increases, the low-voltage differential conductance grows. At large voltages the current saturates, the differential conductance nears zero and even becomes slightly negative for the largest t_C. These features are better brought out in a plot of the differential conductance at finite voltage [Fig. 9(b)]. As we increase the interdot hopping, the zero-bias Kondo anomaly broadens and splits. We can attribute this broadening to the aforementioned increase of the effective Kondo temperature as a function of the interdot hopping. For large interdot tunneling couplings the zero-bias anomaly splits. The splitting of the zero-bias anomaly is an unambiguous indication of quantum coherence between the Kondo states on each dot.

This behavior of the nonlinear transport properties can be better unsderstood in terms of the nonequilibrium DOS on each dot (Figs. 10 and 11).

In Fig. 10, we plot the nonequilibrium DOS ($\mu_L=V/2=12.5T_K^0, \mu_R=-V/2=-12.5T_K^0$) for the left (top figure) and right (bottom figure) coupled quantum dots. For the uncoupled situation ($t_C=0$), each DOS has a Kondo peak around each chemical potential as expected. With increasing interdot hopping, the behavior of each DOS becomes quite complex. The Kondo peak on each side splits into two peaks while at the same time the whole spectral weight near the Fermi level shifts to lower frequencies. Furthermore, these

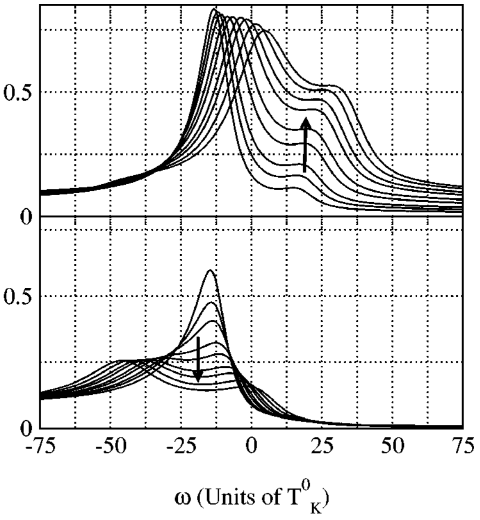

FIG. 11. Nonequilibrium DOS at $t_C = 1.6\Gamma$ for different voltages in the range $V = 10T_K^0$ through $50T_K^0$. $T_K^0 = 0.000\,37\Gamma$. Top: left DOS. Bottom: right DOS. The arrows mark the directions of increasing voltages.

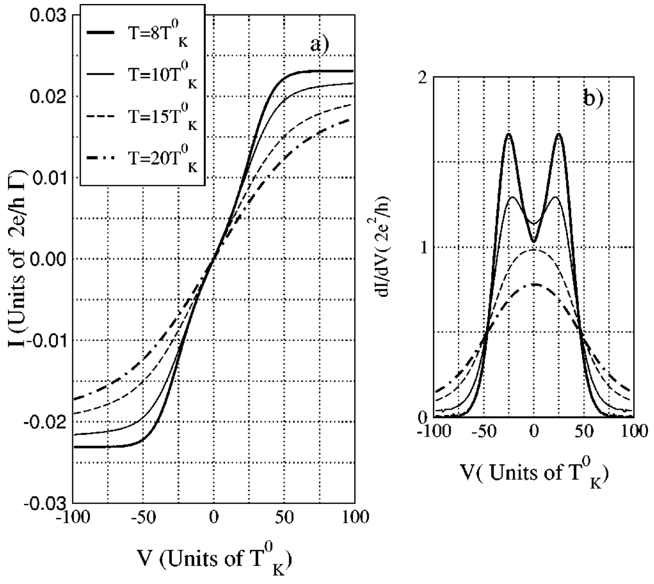

FIG. 12. Nonlinear transport properties of the DQD system ($t_C = 1.6\Gamma$) for different temperatures as a function of the applied bias voltage. $T_K^0 = 0.000\,37\Gamma$. (a) Current-voltage characteristics. (b) Differential conductance at finite voltage.

split peaks are asymmetric, they have different heights and spectral weights (it is important to mention here, however, that the NCA is known to overestimate the asymmetry of the peaks because it does incorrectly treat potential and spin-flip scattering on equal footing.[59]) As the interdot hopping increases, the lower (upper) band of the left (right) DOS moves to lower (higher) frequencies, while increasing its height, until it matches with the upper (lower) band of the right (left) DOS. As an example, for $t_C = 1.6$ the lower peak on the left DOS and the upper peak on the right DOS approximately match at $\omega \sim \mu_R$. As a result, there is a peak in the differential conductance at $V = 25T_K^0$ for this interdot coupling [solid curve of Fig. 9(b)].

Also interesting is to study how the DOS evolves as a function of the applied voltage for a fixed interdot coupling. This nontrivial behavior of the DOS versus applied voltage is studied in Fig. 11 where we plot the nonequilibrium DOS for $t_C = 1.6$ and different voltages from $V = 10T_K^0$ to $V = 50T_K^0$ in intervals of $\Delta V = 5T_K^0$. As the voltage increases, the left (right) DOS moves to higher (lower) frequencies such that the middle point between the split Kondo peaks lies approximately at the left (right) chemical potential (this discussion is only qualitative; note that even for the uncoupled case the Kondo peaks *do not* lie exactly on each chemical potential).

The temperature dependence of the current and differential conductance are plotted in Fig. 12. Several features in these curves are noteworthy. If we focus first in the differential conductance [Fig. 12(b)] we see that the splitting of the zero-bias anomaly can be resolved for temperatures $T \lesssim 10T_K^0$. For higher temperatures the splitting can no longer be resolved and, instead, a broad zero-bias anomaly is obtained. Also important to mention is the nonmonotonic behavior of the linear conductance $\mathcal{G} = dI/dV|_{V=0}$ with temperature. Starting from high temperatures, the linear conductance first *increases* for decreasing temperatures, indicating the appearance of Kondo physics. This behavior saturates at the temperature for which the splitting is resolved (here $T \sim 10T_K^0$) and then the linear conductance *decreases* for decreasing temperatures. This behavior can be easily explained by noting that the linear conductance at finite temperatures is a convolution of the DOS around the Fermi level with the derivative of the Fermi function (whose full width at half maximum is $3.5T$). When the width of the derivative of the Fermi function is smaller than the splitting of the Kondo peak this convolution is very small, due to the small spectral weight around the Fermi level when the Kondo peak splits, explaining why the linear conductance decreases when lowering the temperature. This nonmonotonic temperature behavior is an indirect proof of the formation of the splitting (in single dots in the Kondo regime the linear conductance monotonically increases, until it saturates in the Fermi-liquid regime, for decreasing temperatures). We show this behavior in Fig. 13 where we compare the temperature dependence of the linear conductance of a single quantum dot (solid line) with the temperature dependence of the linear conductance of a double quantum dot with $t_C = 1.6$ (dashed line). The linear conductance for the single dot follows the usual logarithmic increase at intermediate temperatures followed by a saturation near the unitary limit. The linear conductance for the double-dot case shows a nonmonotonic temperature dependence, it increases for decreasing temperatures in the region $T > T^*$ whereas it decreases in the region $T < T^*$. The temperature scale T^* [which is the temperature for which the splitting is resolved in Fig. 12(b)] characterizes quantum coherence between both dots in the Kondo regime. Note that in order to compare with the single-dot case the temperature has been scaled with respect to the Kondo temperature of the *single-dot problem*,

$$T_K = D\sqrt{2\Delta_0/\pi|\epsilon_0|}\exp(-\pi|\epsilon_0|/4\Delta_0).$$

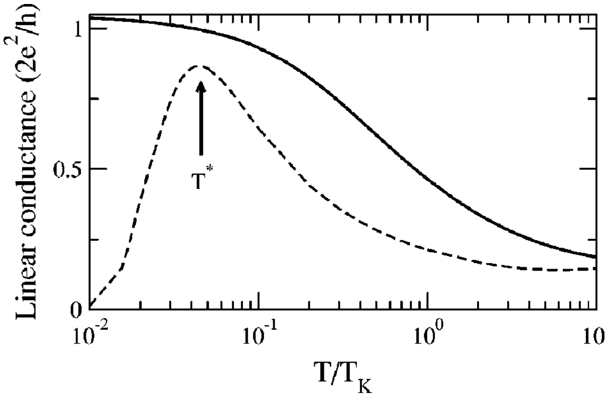

FIG. 13. Comparison of the temperature dependence of the linear conductance in a single quantum dot (solid line) and a double quantum dot with $t_C = 1.6\Gamma$ (dashed line). The linear conductance for the single dot follows the usual logarithmic increase at intermediate temperatures followed by a saturation near the unitary limit. The linear conductance for the double-dot case shows a nonmonotonic temperature dependence, it increases for decreasing temperatures in the region $T > T^*$ whereas it decreases in the region $T < T^*$. The temperature scale T^* characterizes quantum coherence between both dots in the Kondo regime. Note that in order to compare with the single-dot case the temperature has been scaled with respect to the Kondo temperature of the *single-dot problem*, see main text.

Finally, it is important to mention here is that the NCA is known to overestimate the Kondo peak amplitude (and then the linear conductance) when calculated from the density of states. Typical overestimates are within the range 10–15%.[14] Keeping this overestimation in mind (which for temperatures $T \lesssim 4 \times 10^{-2} T_K$ leads to an overshooting of the unitary limit in the single-dot case; Fig. 13, solid line), we purposefully show results at low temperatures where the temperature dependences of the linear conductance for the single- and double-dot cases compare best.

Finally, we comment on the temperature dependence of the differential conductance at large voltages [see Fig. 12(a)]. At low temperatures the slope of the I-V characteristics at large voltages approaches zero and eventually becomes slightly negative, namely, the I-V characteristics present negative differential conductance (NDC), at the lowest temperatures. The slope of the differential conductance increases gradually as one increases the temperature. For the highest temperature studied ($T = 20T_K^0$, dashed-dotted line), no traces of NDC are found even for very large voltages.

This NDC behavior can be physically understood as follows: at low voltages, the current is carried only by spin fluctuations mediated by the Kondo effect between the leads and the dots (without the Kondo effect, the current would be zero due to the Coulomb blockade). As one increases the voltage, the Kondo effect is progressively reduced by voltage-induced decoherence[73] leading to a decrease of spin fluctuations and thus to the current. If thermal and quantum fluctuations were not present the current would go to zero for $V \gg T_K^0$, which is what one gets within the SBMFT, see below. On the contrary, the NCA does include fluctuations which regulate the background current $I \neq 0$ for $T_K^0 \ll V < 2\tilde{\epsilon}_0$ ($\tilde{\epsilon}_0$ is the level position renormalized by charge fluctuations[7]). The mechanism leading to current reduction for increasing voltages, i.e., NDC, thus becomes less and less effective as the applied voltage approaches $2\tilde{\epsilon}_0$, namely, when charge fluctuations do start to play a role, and/or when the temperature increases. We are studying a range of voltages of the I-V characteristics for which $V \ll 2\tilde{\epsilon}_0$ (the largest voltage in Fig. 12 is $V = 100T_K^0$ whereas charge fluctuations appear in an energy range of $\sim 5 \times 10^3 T_K^0$–$5 \times 10^4 T_K^0$, depending on t_C, see Fig. 7), so the NDC is mainly destroyed by thermal fluctuations. This is shown in Fig. 14, where we compare the I-V characteristics [Fig. 14(a)] and differential conductance [Fig. 14(b)] of the system at low ($T = 5T_K^0$) and high ($T = 20T_K^0$) temperatures. For the low-temperature situation, the slope at large voltages does indeed develop NDC for $V \gtrsim 50T_K^0$. At $V \simeq 50T_K^0$, the differential conductance becomes zero and the current smoothly starts to decrease as one increases the dc voltage. For $T = 20T_K^0$, the differential conductance is always positive. This can be easily understood in terms of the increase of the background DOS between $\omega \sim 0$ (spin fluctuations) and $\omega \sim \tilde{\epsilon}_0$ (charge fluctuations) as temperature increases which leads to an increase of the differential conductance.

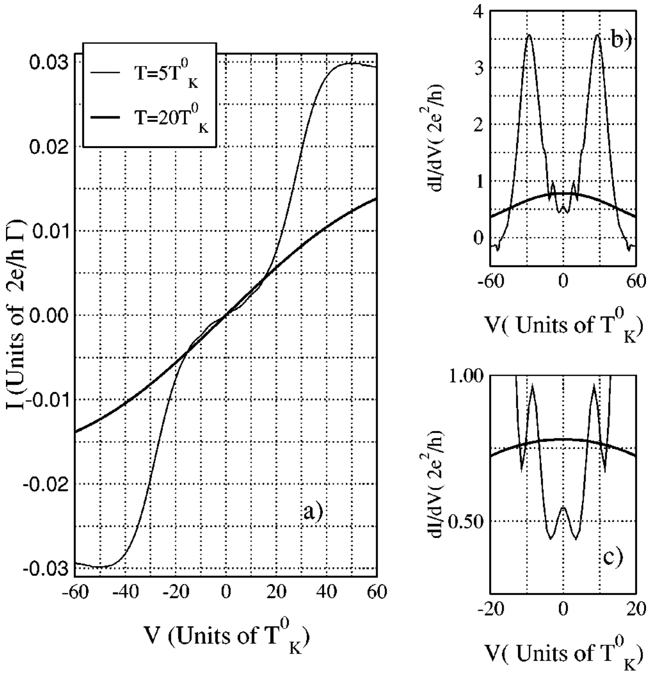

FIG. 14. Nonlinear transport properties of the DQD system ($t_C = 1.6\Gamma$) for two different temperatures as a function of the applied bias voltage. $T_K^0 = 0.000\,37\Gamma$. (a) Current-voltage characteristics. (b) Differential conductance at finite voltage. At large voltages the system develops regions of negative differential conductance (see main text). (c) Blowup of the low-voltage region in the differential conductance. The extra structure at low voltages (small zero-bias anomaly plus satellites) is originating from the splitting due to the applied voltage.

The NDC for $T = 5T_K^0$ changes drastically at larger dc voltages where our numerical results for the current rapidly develop a wiggly pattern (not shown). The appearance of this fluctuating pattern in the numerics is accompanied by a breakdown of current conservation, namely, $J_L = -J_R$ is no longer fulfilled. This could be either due to a NCA breakdown or a dynamical instability, namely, the spontaneous development of a time-dependent current in response to the static applied voltage.[77] Dynamical instabilities, rather typical in nonlinear systems presenting NDC,[78] have been recently reported in single QD's in the Kondo regime.[25–27] It is impossible for us to check this possibility (our numerical scheme is only valid for time-translational invariant situations), and so we choose to show no results for voltages $V > 60T_K^0$ and leave this issue for future investigations.

We finish this part with two remarks. The first is that this NDC has been previously reported in the context of the SBMFT.[47] Importantly, the NDC features obtained here are smooth (the dI/dV evolves from zero to negative values in a smooth manner) and gradually disappear as the temperature increases as we mentioned before. On the contrary, the NDC obtained within the SBMFT consists of sharp transitions between the high and low current regions. These sharp transitions can be attributed to the lack of fluctuations (quantum and thermal) of the boson fields in the SBMFT as already anticipated by us in Ref. 47.

The second remark is that the low-voltage part of the differential conductance curve at the lowest temperature [Fig. 14(c)] does also develop new fine structure (extra peaks). The differential conductance develops a small zero-bias anomaly and satellites separated from zero at $\Delta V \sim \pm 10T_K^0$. These new structures in the differential conductance are in agreement with the ones previously reported in two-level quantum dots[65,46] and coupled quantum dots in the limit of strong interdot repulsion[46] and can be attributed to the extra splitting induced by the applied voltage: the voltage splits the peaks in the left and right spectral functions, and a peak in the differential conductance occurs when these split peaks cross each other. The agreement is only qualitative though. In Refs. 46 and 65 such crossings occur at $\Delta\epsilon = V$, where $\Delta\epsilon$ (a fixed quantity) is the energy separation between *single-particle* levels in the two-level quantum dot[65,46] or the energy separation between the bonding and antibonding levels in the coupled quantum dot system.[46] On the contrary, the peaks in the differential conductance of our calculation appear at much lower-frequency scales. As mentioned before, our calculation includes the strong renormalization of the levels due to electronic correlations and due to the voltage. The crossings, hence, appear at voltages for which $\Delta\tilde{\epsilon}(V) = V$ (namely, $\tilde{\epsilon}_+ + V/2 = \tilde{\epsilon}_- - V/2$), where $\Delta\tilde{\epsilon}(V) = \tilde{\epsilon}_- - \tilde{\epsilon}_+ = 2\tilde{t}_C(V)$ is the voltage-dependent energy separation between the antibonding and bonding combinations of the Kondo peak (which, again, is much smaller than the single-particle splitting $2t_C$).

Figure 15, where we plot the full spectral function at a finite voltage, illustrates this phenomenon. Each peak splits by $\pm V/2$. As a result the full DOS develops four peaks, the combinations $\epsilon_+ \pm V/2$ and $\epsilon_- \pm V/2$, that can be clearly resolved at high enough voltages. These split peaks are marked with asterisks for the highest voltage in the figure, the distance between consecutive peaks is twice the renormalized interdot hopping, and the distance between alternate peaks is the voltage. We mention, in passing, that the observation of this fine structure in the differential conductance would constitute a direct proof of the voltage-induced splitting of the Kondo resonance. Here, the splitting associated with the interdot hopping serves as a testing tool, similarly to that provided by an external magnetic field in single quantum dots[12] (the quantity $\Delta\epsilon$ of our previous discussion being now the Zeeman splitting in a single quantum dot with an external magnetic field) to check the voltage-induced splitting. Different proposals for measuring this voltage-induced splitting are the subject of current active research.[67,83,84]

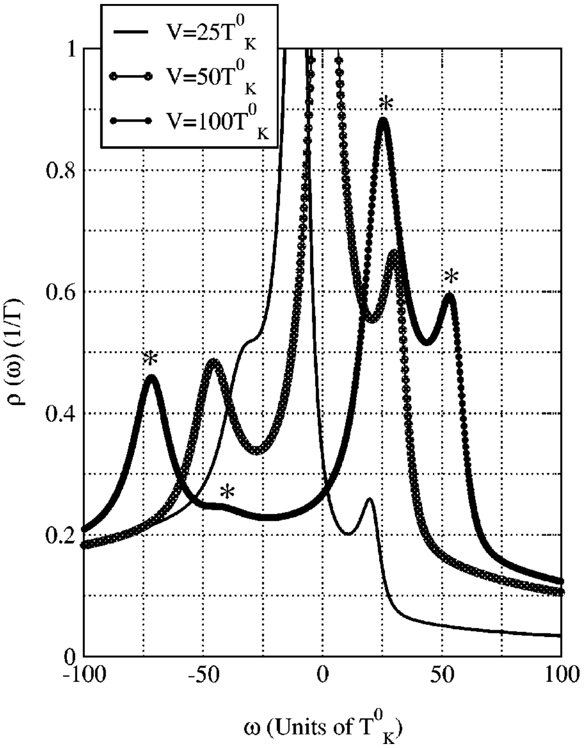

FIG. 15. Nonequilibrium full DOS at low temperature ($T = 5T_K^0$) and $t_C = 1.6\Gamma$ for different voltages $V = 25T_K^0$, $50T_K^0$,$100T_K^0$. $T_K^0 = 0.000\,37\Gamma$. The applied voltage induces extra splittings in the bonding and antibonding combination of the Kondo peak. As a result, four peaks can be clearly resolved in the full DOS at high voltages (these peaks are marked with asterisks for the highest voltage in the figure).

We support our previous paragraph by studying the temperature dependence of the nonequilibrium full DOS at $V = 100T_K^0$ (Fig. 16). At high temperatures, $T \gtrsim 2\tilde{t}_C$, the splitting coming from the interdot coupling cannot be resolved and the coupled dot system is equivalent to a single dot with a broad Kondo peak (coming from a convolution of the bonding and antibonding peaks with thermal broadening). The width of this effective Kondo peak is thus larger than $2\tilde{t}_C$. As expected, a finite voltage, $V > T$, splits this effective single Kondo peak into two peaks separated by V (Fig. 16, thick solid line). Further lowering of the temperature allows to resolve the interdot-induced splitting resulting in extra peaks superimposed to the ones induced by the voltage (Fig. 16, asterisks).

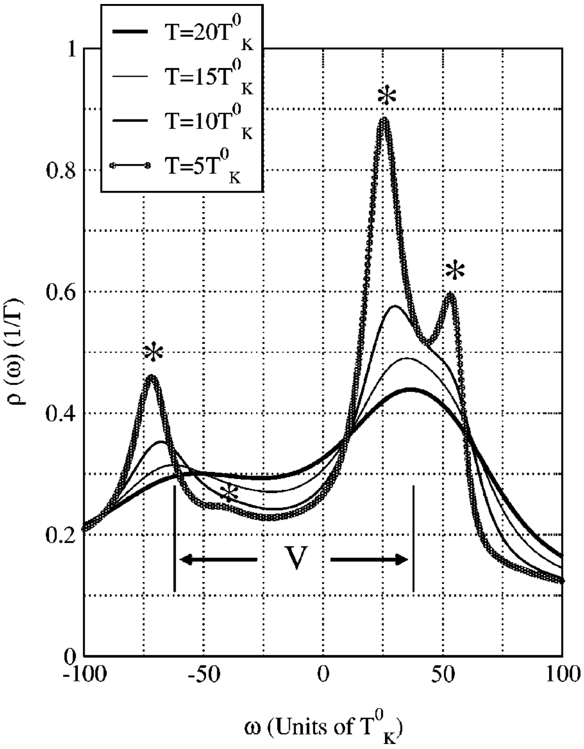

FIG. 16. Temperature dependence of the nonequilibrium full DOS ($V=100T_K^0$) and $t_C=1.6\Gamma$. $T_K^0=0.000\,37\Gamma$. At high temperatures, the splitting coming from the interdot coupling cannot be resolved and the coupled dot system is equivalent to a single dot with a broad Kondo peak coming from a convolution of the bonding and antibonding peaks with thermal broadening. This effective single Kondo peak is split by the voltage as expected (vertical marks). Further lowering of the temperature allows the resolution of the interdot-induced splitting (asterisks).

We finish by commenting on the observability of the effects described in this section: We obtain in our calculations splittings in the differential conductance of the order of $\simeq 50T_K^0$. Typical Kondo temperatures in quantum dots are of the order of a few μeV (for instance, the Kondo temperature is $\simeq 4-250$ μeV in the experiment of Ref. 1), which gives splittings well within the resolution limits of state-of-the-art techniques (remember that 1 μeV$\sim$10 mK).

VI. CONCLUSIONS

We have theoretically studied the transport properties, both equilibrium and out-of-equilibrium properties, of a coupled quantum dot system in the Kondo regime. We have modeled the double quantum dot system by means of a two-impurity Anderson Hamiltonian with interimpurity hopping and infinite on-site interaction on each dot. The Hamiltonian, formulated in slave-boson language, is solved by means of a generalization of the NCA for the present problem: two quantum dots in the Kondo regime, coupled to each other by a tunneling barrier and with an applied voltage across them. We have provided benchmark calculations of the predictions of the noncrossing approximation for the linear and nonlinear transport properties of coupled quantum dots in the Kondo regime. We give a series of predictions that can be observed experimentally in linear and nonlinear transport measurements through coupled quantum dots in the Kondo regime.

(i) The nonlinear differential conductance $\mathcal{G}=dI/dV$ directly measures the transition (as t_C increases) from two isolated Kondo impurities to a coherent bonding and antibonding superposition of the many-body Kondo states of each dot. For increasing interdot couplings, the zero-bias anomaly first broadens and then splits. The latter case corresponds to transport which is optimized for a finite bias voltage matching the splitting between these two bonding and antibonding states.

(ii) The effective Kondo temperature of the coupled system increases with the interdot coupling. This is reflected as a broadening of the zero-bias anomaly.

(iii) The nonmonotonic temperature behavior of the linear conductance $\mathcal{G}=dI/dV|_{V=0}$ is an indirect proof of the formation of the splitting. Starting from high temperatures, the linear conductance first grows for decreasing temperatures, indicating the appearance of Kondo physics. This behavior saturates at the temperature for which the splitting is resolved. Further lowering of the temperature produces a decrease of the linear conductance: The curve linear conductance vs temperature has a maximum at a temperature scale T^* characterizing quantum coherence between the two quantum dots.

(iv) The differential conductance at large voltages can become negative (NDC).

(v) At low enough temperatures, it is possible to resolve extra structures in the differential conductance coming from the splitting induced by the applied bias voltage.

We hope our work will inspire and encourage experimental investigations of Kondo physics in coupled quantum dots and related systems.

ACKNOWLEDGMENTS

We are thankful to Piers Coleman, Chris Hooley, and Olivier Parcollet for many useful and stimulating discussions during the first stages of this work. This work was supported by the NSF Grant No. DMR 00-93079, U.S. DOE Grant No. DE-FG02-99ER45970, and by the MEC of Spain Grant No. PF 98-07497938. R.A. acknowledges support from the MCYT of Spain through the ‘‘Ramón y Cajal’’ program for young researchers.

APPENDIX A: BAYM FUNCTIONAL AND NCA SELF-ENERGIES

The NCA technique is the lowest-order fully conserving and self-consistent theory one can construct from a Baym functional Φ.[56] This functional is defined as the set of diagrams consisting of all vacuum skeleton diagrams built out of fully renormalized Green's functions and the bare vertex. Using this definition, we obtain to lowest order in the lead-dot coupling the functional Φ_1 [Fig. 3(a)] which can be written as.

$$\Phi_1 = i\frac{V^2}{N}\sum_{\alpha\in\{L,R\}}\sum_{k_\alpha}\sum_{\sigma}\int_c d\tau d\tau' \times G_{\alpha\sigma}(\tau,\tau')g_{k_\alpha,\sigma}(\tau',\tau)B_\alpha(\tau',\tau), \qquad \text{(A1)}$$

where the integrals and the time-ordered Green's functions

$$iG_{\alpha\sigma}(\tau,\tau')\equiv\langle T_c f_{\alpha\sigma}(\tau)f^\dagger_{\alpha\sigma}(\tau')\rangle,$$

$$iB_\alpha(\tau,\tau')\equiv\langle T_c b_\alpha(\tau)b^\dagger_\alpha(\tau')\rangle,$$

$$ig_{k_\alpha,\sigma}(\tau,\tau')\equiv\langle T_c c_{k_\alpha,\sigma}(\tau)c^\dagger_{k_\alpha,\sigma}(\tau')\rangle, \qquad \text{(A2)}$$

are defined along a complex contour.

The self-energies are obtained by the functional derivation of the Baym functional,

$$\Sigma^{(1)}_{\alpha\sigma}(\tau,\tau') = \frac{\partial\Phi_1}{\partial G_{\alpha\sigma}(\tau,\tau')},$$

$$\Pi^{(1)}_{\alpha}(\tau,\tau') = \frac{\partial\Phi_1}{\partial B_{\alpha}(\tau,\tau')}, \qquad \text{(A3)}$$

which gives

$$\Sigma^{(1)}_{L(R)\sigma}(\tau,\tau') = i\frac{V^2}{N}\sum_{k_{L(R)}} g_{k_{L(R)}\sigma}(\tau,\tau')B_{L(R)}(\tau,\tau'),$$

$$\Pi^{(1)}_{L(R)}(\tau,\tau') = -i\frac{V^2}{N}\sum_{\sigma}\sum_{k_{L(R)}} g_{k_{L(R)}\sigma}(\tau',\tau)G_{L(R)\sigma}(\tau,\tau'). \qquad \text{(A4)}$$

A similar analysis on Φ_2 [interdot term, Fig. 3(b)] gives

$$\Phi_2 = -\left(\frac{t_C}{N}\right)^2\sum_{\sigma}\int_c d\tau d\tau' G_{L\sigma}(\tau,\tau')B_L(\tau',\tau) \times G_{R\sigma}(\tau,\tau')B_R(\tau',\tau), \qquad \text{(A5)}$$

$$\Sigma^{(2)}_{L(R)\sigma}(\tau,\tau') = -\left(\frac{t_C}{N}\right)^2 B_{L(R)}(\tau,\tau')G_{R(L)\sigma}(\tau,\tau') \times B_{R(L)}(\tau',\tau),$$

$$\Pi^{(2)}_{L(R)}(\tau,\tau') = \left(\frac{t_C}{N}\right)^2\sum_{\sigma} G_{R(L)\sigma}(\tau',\tau)B_{R(L)}(\tau,\tau') \times G_{L(R)\sigma}(\tau,\tau'). \qquad \text{(A6)}$$

The final NCA self-energies are thus

$$\Sigma^{(NCA)}_{L(R)\sigma}(\tau,\tau') = \Sigma^{(1)}_{L(R)\sigma}(\tau,\tau') + \Sigma^{(2)}_{L(R)\sigma}(\tau,\tau'), \qquad \text{(A7)}$$

and

$$\Pi^{(NCA)}_{L(R)}(\tau,\tau') = \Pi^{(1)}_{L(R)}(\tau,\tau') + \Pi^{(2)}_{L(R)}(\tau,\tau'). \qquad \text{(A8)}$$

Finally, continuation to the real time domain of the self-energies $\Sigma^{(NCA)}$ and $\Pi^{(NCA)}$ and specialization to steady state give Eqs. (10) and (11) in the main text.

APPENDIX B: EQUATION OF MOTION FOR THE CONTOUR-ORDERED OFF-DIAGONAL GREEN'S FUNCTIONS

In this appendix, we discuss the equation of motion for the contour-ordered Green's functions and show explicitly that their off-diagonal components vanish for $t_C=0$. As a consequence, the off-diagonal self-energies (Sec. IV A) do not contribute to order t_C^2 and can be neglected within the NCA.

We start from the definition of the contour-ordered Green's function,

$$G^t_{\alpha\sigma,\alpha'\sigma}(t-t') = -i\langle T_c f_{\alpha\sigma}(t)f^\dagger_{\alpha'\sigma}(t')\rangle, \qquad \text{(B1)}$$

and its equation of motion

$$-i\frac{\partial}{\partial t'}G^t_{\alpha\sigma,\alpha'\sigma}(t-t') = \delta(t-t')\langle\{f_{\alpha\sigma}(t),f^\dagger_{\alpha'\sigma}(t')\}\rangle - i\langle T_c f_{\alpha\sigma}(t)[H,f^\dagger_{\alpha'\sigma}(t')]\rangle, \qquad \text{(B2)}$$

where $\{,\}$ and $[,]$ denote anticommutation and commutation, respectively. As we mentioned in Sec. III, the time-ordering operator T_c operates along a contour c in the complex plane. The anticommutator for $\alpha\neq\alpha'$ is zero, and the equation of motion for the off-diagonal Green's functions becomes

$$-i\frac{\partial}{\partial t'}G^t_{\alpha\sigma,\alpha'\sigma}(t-t') = -i\langle T_c f_{\alpha\sigma}(t)[H,f^\dagger_{\alpha'\sigma}(t')]\rangle \quad \text{for} \quad \alpha\neq\alpha'. \qquad \text{(B3)}$$

For instance, the LR component can be written as

$$\left(-i\frac{\partial}{\partial t'}-\epsilon_R\right)G^t_{L\sigma,R\sigma}(t-t') = -i\frac{V}{\sqrt{N}}\sum_{k_R}\langle T_c f_{L\sigma}(t)c^\dagger_{k_{R\sigma}}(t')b^\dagger_R(t')\rangle - i\frac{t_C}{N}\langle T_c f_{L\sigma}(t)f^\dagger_{L\sigma}(t')b_L(t')b^\dagger_R(t')\rangle. \qquad \text{(B4)}$$

By operating with g^t_R from right, the LR contour-ordered Green's function can be expressed as the sum of two terms,

$$G^t_{L\sigma,R\sigma}(t-t') = G^{(1)t}_{L\sigma,R\sigma}(t-t') + G^{(2)t}_{L\sigma,R\sigma}(t-t'). \qquad \text{(B5)}$$

The first one

$$G^{(1)t}_{L\sigma,R\sigma}(t-t') = \frac{V}{\sqrt{N}}\sum_{k_R}\int_c d\tau C^t_{k_R,L}(t-\tau)g^t_R(\tau-t') \qquad \text{(B6)}$$

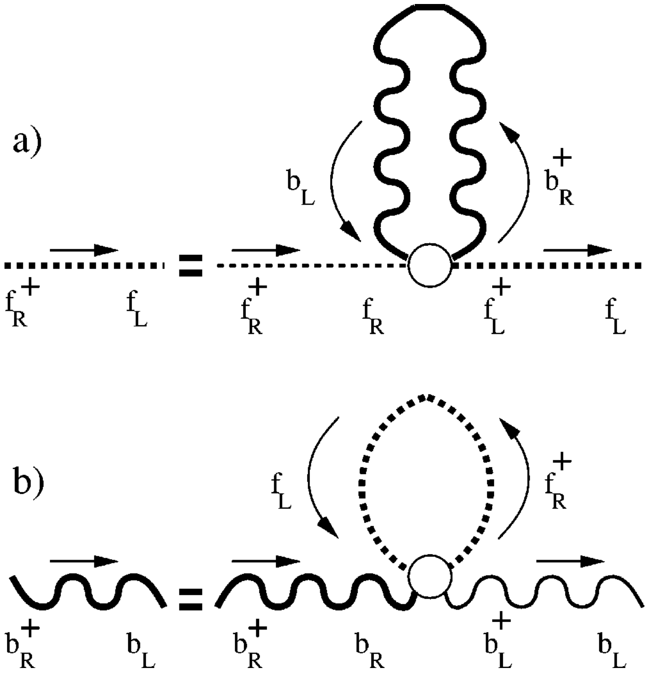

FIG. 17. Feynman diagrams corresponding to (a) the off-diagonal fermion propagator of Eq. (B7) (schematically $G_{LR} = G_{LL}B_{LR}g_{RR}$) and (b) the off-diagonal boson propagator of Eq. (B8) (schematically $B_{LR} = b_{LL}G_{LR}B_{RR}$).

contains the off-diagonal Green's function

$$C^t_{k_R,LR}(t-\tau) = -i\langle T_c f_{L\sigma}(t) c^\dagger_{k_{R\sigma}}(\tau) b^\dagger_R(\tau)\rangle,$$

which contains high-order terms involving both interdot and dot-lead couplings (for example, when $t > \tau$, in the contour sense, this correlation function represents the creation of an electron at the *right* lead followed by the annihilation of another electron in the *left* dot at a later time). We disregard these kind of terms in the following in order to simplify our discussion.

The second term in Eq. (B5) is

$$G^{(2)t}_{L\sigma,R\sigma}(t-t') = \frac{t_C}{N}\int_c d\tau D^t_{LR}(t-\tau) g^t_R(\tau-t'), \qquad \text{(B7)}$$

which contains the off-diagonal Green's function

$$D^t_{LR}(t-\tau) = -i\langle T_c f_{L\sigma}(t) f^\dagger_{L\sigma}(\tau) b_L(\tau) b^\dagger_R(\tau)\rangle.$$

The two-particle Green's function $D^t_{LR}(t-\tau)$ can be expressed within the NCA as the product of one diagonal fermion propagator (the left one in this particular example) and one off-diagonal bosonic propagator. This allows us to express diagrammatically Eq. (B7) as in Fig. 17(a).

The boson off-diagonal Green's function can be obtained using a similar analysis:

$$B^{(2)t}_{L,R}(t-t') = \frac{t_C}{N}\sum_\sigma \int d\tau b^t_L(t-\tau) F^t_{L\sigma,R\sigma}(\tau-t'), \qquad \text{(B8)}$$

with

$$F^t_{L\sigma,R\sigma}(\tau-t') = -i\langle T_c f^\dagger_{R\sigma}(\tau) b_R(\tau) f_{L\sigma}(\tau) b^\dagger_R(t')\rangle.$$

Again, the two-particle Green's function $F^t_{L\sigma,R\sigma}(\tau-t')$ can be decomposed as the product of a fermionic (off-diagonal) and a bosonic (diagonal) propagator, allowing us to express diagrammatically Eq. (B8) as in Fig. 17(b).

In the diagrams of Fig. 17, the off-diagonal fermion and boson propagators are coupled; importantly, both vanish for $t_C = 0$ [of course the off-diagonal propagators not considered in this discussion, such as the one in Eq. (B6), would also be zero without the interdot coupling]. In particular, this implies that the off-diagonal self-energies also vanish to order t_C^2 (they are built out of *bare* off-diagonal propagators) as stated in Sec. IV A.

A possible confusing point is that in the usual formulation it would be necessary to use the off-diagonal self-energies and propagators in the noninteracting problem. In that problem, there are no slave bosons, and so no possibility for the self-energy diagrams of Fig. 17. However, the slave propagators in Fig. 4(b) are also stripped away. According to the usual definitions, Fig. 4(b) no longer remains a proper self-energy insertion, and one would need the off-diagonal propagators to lowest order in the tunneling. However, a moments reflection shows that the same result is obtained without the off-diagonal propagators, if one *defines* the "proper" self-energy with the requirement that it should begin and end on the same lead, and takes the dashed line in Fig. 4(b) to be the propagator in the absence of the interdot coupling.

APPENDIX C: PROJECTION

Here we discuss the evaluation of operator averages within the restricted subspace of the Hilbert space with the constraints of Eq. (3). The formal expression for the expectation value of an operator in this subspace can be written as:

$$\langle \hat{O}\rangle_{Q_L=1,Q_R=1} = \frac{1}{Z_{Q_L=1,Q_R=1}}\mathrm{Tr}\{e^{-\beta(H_0-\mu_L N_L-\mu_R N_R)} \times \delta_{Q_L,1}\delta_{Q_R,1}T_C[S_C(-\infty,\infty)\hat{O}]\}, \qquad \text{(C1)}$$

where T_C orders operators along a complex contour, the hopping terms are treated as perturbations (i.e., H_0 contains the isolated regions of the problem, leads and dots, before they are connected), and the partition function is given by

$$Z_{Q_L=1,Q_R=1} = \mathrm{Tr}\{e^{-\beta(H_0-\mu_L N_L-\mu_R N_R)} \times \delta_{Q_L,1}\delta_{Q_R,1}T_C[S_C(-\infty,\infty)]\}. \qquad \text{(C2)}$$

Since the charge operators commute with the Hamiltonian, each constraint can be incorporated by a Kronecker δ function in the statistical averages of Eqs. (C1) and (C2). To relate averages in the restricted ensemble with the ones corresponding to an unrestricted ensemble, we represent each Kronecker δ function as an integral over a complex chemical potential[14,54] (see also Appendix D in Ref. 50 and chap. 7 of Ref. 7):

$$\delta_{Q_L,1}=\frac{\beta}{2\pi}\int_{-\pi/\beta}^{\pi/\beta}d\lambda_L e^{-i\beta\lambda_L(Q_L-1)},$$

$$\delta_{Q_R,1}=\frac{\beta}{2\pi}\int_{-\pi/\beta}^{\pi/\beta}d\lambda_R e^{-i\beta\lambda_R(Q_R-1)}, \tag{C3}$$

$$\langle\hat{O}\rangle_{Q_L=1,Q_R=1}=\frac{1}{Z_{Q_L=1,Q_R=1}}\left(\frac{\beta}{2\pi}\right)^2\int_{-\pi/\beta}^{\pi/\beta}d\lambda_L \times\int_{-\pi/\beta}^{\pi/\beta}d\lambda_R e^{i\beta\lambda_L}e^{i\beta\lambda_R}Z_{GC}\langle\hat{O}\rangle_{GC}. \tag{C4}$$

This way, we can relate the average in the constrained ensemble with an average in the grand canonical ensemble which can be written as

$$\langle\hat{O}\rangle_{GC}=\frac{1}{Z_{GC}}\mathrm{Tr}\{e^{-\beta(H_0-\mu_LN_L-\mu_RN_R+i\lambda_LQ_L+i\lambda_RQ_R)}\times T_C[S_C(-\infty,\infty)\hat{O}]\},$$

$$Z_{GC}=\mathrm{Tr}\{e^{-\beta(H_0-\mu_LN_L-\mu_RN_R+i\lambda_LQ_L+i\lambda_RQ_R)}\times T_C[S_C(-\infty,\infty)]\}. \tag{C5}$$

This average inside the integral in Eq. (C4) now obeys a linked cluster theorem and we can use conventional field theory. In principle, we can stop here, evaluate the averages in the grand canonical ensemble, and project to the physical ensemble by a final integration over the chemical potentials. Further simplification can be gained, however, by noting that the grand canonical partition function Z_{GC} can be rewritten as a sum over canonical partition functions:

$$Z_{GC}=\sum_{Q_L=0}^{\infty}\sum_{Q_R=0}^{\infty}Z_C(Q_L,Q_R)e^{-i\beta\lambda_LQ_L}e^{-i\beta\lambda_RQ_R} \tag{C6}$$

and by expanding the expressions in the grand canonical ensemble as power series,

$$Z_{GC}=Z_C(0,0)+Z_C(1,0)e^{-i\beta\lambda_L}+Z_C(0,1)e^{-i\beta\lambda_R}+Z_C(1,1)e^{-i\beta\lambda_L}e^{-i\beta\lambda_R}+\cdots,$$

$$\langle\hat{O}\rangle_{GC}=\langle\hat{O}\rangle^{0,0}+\langle\hat{O}\rangle^{1,0}e^{-i\beta\lambda_L}+\langle\hat{O}\rangle^{0,1}e^{-i\beta\lambda_R}+\langle\hat{O}\rangle^{1,1}e^{-i\beta\lambda_L}e^{-i\beta\lambda_R}+\cdots. \tag{C7}$$

Inserting these power-series expansions inside the integral in Eq. (C4), the only terms that survive are:

$$\langle\hat{O}\rangle_{Q_L=1,Q_R=1}=\frac{1}{Z_C(1,1)}[Z_C(0,0)\langle\hat{O}\rangle^{1,1}+Z_C(1,0)\langle\hat{O}\rangle^{0,1}+Z_C(0,1)\langle\hat{O}\rangle^{1,0}], \tag{C8}$$

where we have used $\langle\hat{O}\rangle^{0,0}=0$ which is the case for any physical operator of interest. The operators we are interested in can be classified as operators acting on the left dot or operators acting on the right dot,[85] namely,

$$\langle\hat{O}_L\rangle_{Q_L=1,Q_R=1}=\left[\frac{Z_C(0,1)}{Z_C(1,1)}\langle\hat{O}_L\rangle^{1,0}+\frac{Z_C(0,0)}{Z_C(1,1)}\langle\hat{O}_L\rangle^{1,1}\right],$$

$$\langle\hat{O}_R\rangle_{Q_L=1,Q_R=1}=\left[\frac{Z_C(1,0)}{Z_C(1,1)}\langle\hat{O}_R\rangle^{0,1}+\frac{Z_C(0,0)}{Z_C(1,1)}\langle\hat{O}_R\rangle^{1,1}\right]. \tag{C9}$$

We can conclude from this analysis that physical operators on the left and right sides have to be of the order of $O(e^{-i\beta\lambda_L})+O(e^{-i\beta\lambda_L}e^{-i\beta\lambda_R})$ and $O(e^{-i\beta\lambda_R})+O(e^{-i\beta\lambda_L}e^{-i\beta\lambda_R})$, respectively. From now on we denote the order of the operators as $O(1,0)+O(1,1)$ (left operators) and $O(0,1)+O(1,1)$ (right operators).

Equations (C9) can be rewritten as

$$\langle\hat{O}_L\rangle_{Q_L=1,Q_R=1}=\frac{Z_C(0,1)}{Z_C(1,1)}\left[\langle\hat{O}_L\rangle^{1,0}+\frac{Z_C(0,0)}{Z_C(0,1)}\langle\hat{O}_L\rangle^{1,1}\right],$$

$$\langle\hat{O}_R\rangle_{Q_L=1,Q_R=1}=\frac{Z_C(1,0)}{Z_C(1,1)}\left[\langle\hat{O}_R\rangle^{0,1}+\frac{Z_C(0,0)}{Z_C(1,0)}\langle\hat{O}_R\rangle^{1,1}\right]. \tag{C10}$$

The coefficients $Z_C(0,1)/Z_C(0,0)$ and $Z_C(1,0)/Z_C(0,0)$ can be identified with the right and left normalization factors in the absence of the interdot hopping, i.e., $Z_C(0,0)/Z_C(0,1)\equiv 1/Z_R$ and $Z_C(0,0)/Z_C(1,0)\equiv 1/Z_L$ and can be obtained from the left and right canonical partition functions of two independent single-impurity problems at different chemical potentials μ_L and μ_R, respectively (see Refs. 14, 62, and 68). This way, the physical operators in the constrained ensemble can be written as

$$\langle\hat{O}_L\rangle_{Q_L=1,Q_R=1}=\frac{Z_C(0,1)}{Z_C(1,1)}\left[\langle\hat{O}_L\rangle^{1,0}+\frac{1}{Z_R}\langle\hat{O}_L\rangle^{1,1}\right],$$

$$\langle\hat{O}_R\rangle_{Q_L=1,Q_R=1}=\frac{Z_C(1,0)}{Z_C(1,1)}\left[\langle\hat{O}_R\rangle^{0,1}+\frac{1}{Z_L}\langle\hat{O}_R\rangle^{1,1}\right]. \tag{C11}$$

Equation (C11) is the central result of this section. Left (right) physical operators in the restricted ensemble with $Q_L=1,Q_R=1$ contain two terms: (i) the coefficient of the term of the order of $O(e^{-i\beta\lambda_{L(R)}})$ in the operator evaluated in the grand canonical ensemble plus (ii) the coefficient of the term of the order of $O(e^{-i\beta\lambda_L}e^{-i\beta\lambda_R})$ in the operator evaluated in the grand canonical ensemble divided by the normalization factor of the right (left) problem without the interdot coupling.

The new normalization factors, $Z_C(0,1)/Z_C(1,1)$ and $Z_C(1,0)/Z_C(1,1)$ can be obtained from the identities $\langle\hat{Q}_L\rangle_{Q_L=1,Q_R=1}\equiv 1$ and $\langle\hat{Q}_R\rangle_{Q_L=1,Q_R=1}\equiv 1$.

Now, we apply the previous projection procedure to the self-energies of Eqs. (10) and (11). The projection of the self-energies can be accomplished in three basic steps. In a first step, we follow Langreth and Nordlander in Ref. 62 (see also Ref. 14): since the Dyson equations for $G^<_{L(R)}$ and $B^<_{L(R)}$ contain either $G^<_{L(R)}$ or $B^<_{L(R)}$ in every term, the self-energies that multiply these quantities must have all terms proportional to $G^{<}_{L(R)}$ or $B^{<}_{L(R)}$ or higher projected out. As a result we obtain from Eqs. (10) and (11) the following self-energies $(\tau=t-t')$:

$$\Sigma^{r}_{L(R),\sigma}(\tau)=\left\{\frac{1}{N}\tilde{K}^{>}_{L(R),\sigma}(\tau)+i\left(\frac{t_C}{N}\right)^2[\tilde{G}^{r}_{R(L),\sigma}(\tau)-\tilde{G}^{a}_{R(L),\sigma}(\tau)]\tilde{B}^{<}_{R(L)}(-\tau)\right\}B^{r}_{L(R)}(\tau),$$

$$\Pi^{r}_{L(R)}(\tau)=\left\{\frac{1}{N}\sum_{\sigma}\tilde{K}^{<}_{L(R),\sigma}(-\tau)+i\left(\frac{t_C}{N}\right)^2\sum_{\sigma}[\tilde{B}^{r}_{R(L)}(\tau)-\tilde{B}^{a}_{R(L)}(\tau)]\tilde{G}^{<}_{R(L),\sigma}(-\tau)\right\}G^{r}_{L(R),\sigma}(\tau). \quad \text{(C12)}$$

Similarly,

$$\Sigma^{<}_{L(R),\sigma}(\tau)=\left\{\frac{1}{N}\tilde{K}^{<}_{L(R),\sigma}(\tau)+i\left(\frac{t_C}{N}\right)^2\tilde{G}^{<}_{R(L),\sigma}(\tau)[\tilde{B}^{r}_{R(L)}(-\tau)-\tilde{B}^{a}_{R(L)}(-\tau)]\right\}B^{<}_{L(R)}(\tau),$$

$$\Pi^{<}_{L(R)}(\tau)=\left\{\frac{1}{N}\sum_{\sigma}\tilde{K}^{>}_{L(R),\sigma}(-\tau)+i\left(\frac{t_C}{N}\right)^2\sum_{\sigma}\tilde{B}^{<}_{R(L)}(\tau)\times[\tilde{G}^{r}_{R(L),\sigma}(-\tau)-\tilde{G}^{a}_{R(L),\sigma}(-\tau)]\right\}G^{<}_{L(R),\sigma}(\tau), \quad \text{(C13)}$$

where we have emphasized in our notation the structure $(\text{Kernel}^{(1)}+\text{Kernel}^{(2)})\times$propagator. In Kernel$^{(1)}$, the quantities $\tilde{K}$ are defined in terms of the Fourier transforms of the *bare* conduction-electron propagators (namely, without dot-lead coupling) as $\tilde{K}^{\gtrless}_{\alpha,\sigma}(\epsilon)=2\pi\Sigma_{k_\alpha}V^2\delta(\epsilon-\epsilon_{k_\alpha})f^{\gtrless}_{\alpha}(\epsilon)$, where $f^{<}_{\alpha}(\epsilon)=1/(e^{\beta(\epsilon-\mu_\alpha)}+1)$ is the Fermi function and $f^{>}_{\alpha}(\epsilon)=1-f^{<}_{\alpha}(\epsilon)$ (see Ref. 62 and below). This way, the kernel is $O(0{,}0)$. The Green's functions within the Kernel$^{(2)}$ part, namely $\tilde{G}$, $\tilde{B}$, *do not* include the interdot hopping meaning that the kernel is $O(0{,}1)$ for the left part and $O(1{,}0)$ for the right one. This previous projection in the kernels is completely equivalent to the projection one does in the single- impurity problem: with the same kind of arguments one neglects terms of order $O(e^{-i\beta\lambda})$ in the conduction electron propagator which, in principle, is a full propagator to be calculated in the presence of slave fermions and bosons. The self-energy corrections to the lead electron propagators such as the bubble diagram in Fig. 18 are thrown away in the single-impurity case (and also, of course, in our case). As a consequence of this projection, one always works with *bare* conduction-electron propagators, which, again, is not what one gets initially from the unprojected NCA equations.

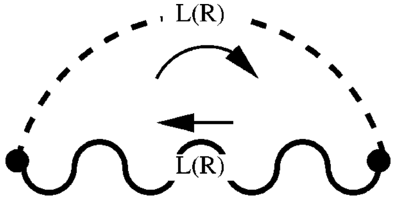

FIG. 18. Self-energy contribution of the order of $O(e^{-i\beta\lambda})$ to the conduction-electron propagator which is projected out by the constraint. The inclusion of this self-energy contribution to the conduction-electron propagator would give unwanted contributions of the order of $O(1{,}0)$ (left contact) and $O(0{,}1)$ (right contact).

In a second step, we project out unwanted contributions from the propagators multiplying the kernels. As we mentioned previously, the left (right) kernel is of the order of $O(0{,}0)+O(0{,}1)$ $[O(0{,}0)+O(1{,}0)]$, meaning that the retarded propagators multiplying these kernels, Eq. (C12), should be of the order of $O(0{,}0)$, namely, *bare* propagators with respect to the interdot. The corresponding lesser propagators in Eq. (C13) therefore contribute with $O(1{,}0)$ (left operators) and $O(0{,}1)$ (right operators) giving the correct order: $O(1{,}0)+O(1{,}1)$ for the left operators and $O(0{,}1)+O(1{,}1)$ for the right ones. Finally, according to Eq. (C11) the $O(1{,}1)$ contributions should be normalized by Z_R and Z_L, respectively. The final set of the projected self-energies is then

$$\Sigma^{r}_{L(R),\sigma}(\tau)=\left\{\frac{1}{N}\tilde{K}^{>}_{L(R),\sigma}(\tau)+i\left(\frac{t_C}{N}\right)^2[\tilde{G}^{r}_{R(L),\sigma}(\tau)-\tilde{G}^{a}_{R(L),\sigma}(\tau)]\frac{\tilde{B}^{<}_{R(L)}(-\tau)}{Z_{R(L)}}\right\}\tilde{B}^{r}_{L(R)}(\tau),$$

$$\Pi^{r}_{L(R)}(\tau)=\left\{\frac{1}{N}\sum_{\sigma}\tilde{K}^{<}_{L(R),\sigma}(-\tau)+i\left(\frac{t_C}{N}\right)^2\sum_{\sigma}[\tilde{B}^{r}_{R(L)}(\tau)-\tilde{B}^{a}_{R(L)}(\tau)]\frac{\tilde{G}^{<}_{R(L),\sigma}(-\tau)}{Z_{R(L)}}\right\}\tilde{G}^{r}_{L(R),\sigma}(\tau), \quad \text{(C14)}$$

$$\Sigma^{<}_{L(R),\sigma}(\tau)=\left\{\frac{1}{N}\tilde{K}^{<}_{L(R),\sigma}(\tau)+i\left(\frac{t_C}{N}\right)^2\frac{\tilde{G}^{<}_{R(L),\sigma}(\tau)}{Z_{R(L)}}\times[\tilde{B}^{r}_{R(L)}(-\tau)-\tilde{B}^{a}_{R(L)}(-\tau)]\right\}\tilde{B}^{<}_{L(R)}(\tau),$$

$$\Pi^{<}_{L(R)}(\tau)=\left\{\frac{1}{N}\sum_{\sigma}\tilde{K}^{>}_{L(R),\sigma}(-\tau)+i\left(\frac{t_C}{N}\right)^2\sum_{\sigma}\frac{\tilde{B}^{<}_{R(L)}(\tau)}{Z_{R(L)}}\times[\tilde{G}^{r}_{R(L),\sigma}(-\tau)-\tilde{G}^{a}_{R(L),\sigma}(-\tau)]\right\}\tilde{G}^{<}_{L(R),\sigma}(\tau), \quad \text{(C15)}$$

which correspond to Eqs. (19) and (20) used in the main text.

*Electronic address: raguado@icmm.csic.es

[1] D. Goldhaber-Gordon, H. Shtrikman, D. Mahalu, D. Abusch-Magder, U. Meirav, and M.A. Kastner, Nature (London) **391**, 156 (1998); D. Goldhaber-Gordon, J. Göres, M.A. Kastner, Hadas Shtrikman, D. Mahalu, and U. Meirav, Phys. Rev. Lett. **81**, 5225 (1998).

[2] S.M. Cronenwett, T.H. Oosterkamp, and L.P. Kouwenhoven, Science (Washington, DC, U.S.) **281**, 540 (1998).

[3] J. Schmid, J. Weis, K. Eberl, and K.v. Klitzing, Physica B **256-258**, 182 (1998); Phys. Rev. Lett. **84**, 5824 (2000).

[4] F. Simmel, R.H. Blick, J.P. Kotthaus, W. Wegscheider, and M. Bichler, Phys. Rev. Lett. **83**, 804 (1999).

[5] W.G. van der Wiel, S. De Franceschi, T. Fujisawa, J.M. Elzerman, S. Tarucha, and L.P. Kouwenhoven, Science (Washington, DC, U.S.) **289**, 2105 (2000).

[6] Our work focus on transport properties of lateral quantum dots, small regions lithographically defined on two-dimensional electron gases. Other configurations, also termed quantum dots, include nanocrystals, self-assembled quantum dots, and vertical quantum dots. See, A.P. Alivisatos, Science (Washington, DC, U.S.) **271**, 933 (1996); Leo P. Kouwenhoven, Charles M. Marcus, Paul L. McEuen, Seigo Tarucha, Robert M. Westervelt, and Ned S. Wingreen, in *Mesoscopic Electron Transport*, edited by L. L. Sohn, L. P. Kouwenhoven, and G. Schön (Kluwer, The Netherlands, 1997).

[7] A. C. Hewson, *The Kondo Problem to Heavy Fermions* (Cambridge University Press, Cambridge, 1993).

[8] R.A. Logan and J.M. Rowell, Phys. Rev. Lett. **13**, 404 (1964); A.F.G. Wyatt, *ibid.* **13**, 401 (1964); J. Schewchun and R.M. Williams, *ibid.* **15**, 160 (1965).

[9] D.C. Ralph and R.A. Buhrman, Phys. Rev. Lett. **72**, 3401 (1994).

[10] T.K. Ng and P.A. Lee, Phys. Rev. Lett. **61**, 1768 (1988); L.I. Glazman and M.E. Raikh, JETP Lett. **47**, 452 (1988); A. Kawabata, J. Phys. Soc. Jpn. **60**, 3222 (1991).

[11] Selman Hershfield, John H. Davies, and John W. Wilkins, Phys. Rev. Lett. **67**, 3720 (1991); Phys. Rev. B **46**, 7046 (1992).

[12] Y. Meir, Ned S. Wingreen, and Patrick A. Lee, Phys. Rev. Lett. **70**, 2601 (1993).

[13] A.L. Yeyati, A. Martín-Rodero, and F. Flores, Phys. Rev. Lett. **71**, 2991 (1993).

[14] Ned S. Wingreen and Yigal Meir, Phys. Rev. B **49**, 11040 (1994).

[15] Noam Sivan and Ned S. Wingreen, Phys. Rev. B **54**, 11622 (1996).

[16] J. König, J. Schmid, H. Schoeller, and G. Schön, Phys. Rev. B **54**, 16820 (1996).

[17] P. Coleman, C. Hooley, and O. Parcollet, Phys. Rev. Lett. **86**, 4088 (2001); A. Rosch, J. Paaske, J. Kroha, and P. Wölfle, Phys. Rev. Lett. **90**, 07684 (2003); O. Parcollet and C. Hooley, Phys. Rev. B **66**, 085315 (2002); P. Coleman and W. Mao, cond-mat/0203001 (unpublished).

[18] M.H. Hettler and H. Schoeller, Phys. Rev. Lett. **74**, 4907 (1995).

[19] T.K. Ng, Phys. Rev. Lett. **76**, 487 (1996).

[20] A. Schiller and S. Hershfield, Phys. Rev. Lett. **77**, 1821 (1996).

[21] Rosa López, Ramón Aguado, Gloria Platero, and Carlos Tejedor, Phys. Rev. Lett. **81**, 4688 (1998); Phys. Rev. B **64**, 075319 (2001).

[22] Y. Goldin and Y. Avishai, Phys. Rev. Lett. **81**, 5394 (1998).

[23] A. Kaminski, Yu V. Nazarov, and L.I. Glazman, Phys. Rev. Lett. **83**, 384 (1999); Phys. Rev. B **62**, 8154 (2000).

[24] Peter Nordlander, Ned S. Wingreen, Yigal Meir, and David C. Langreth, Phys. Rev. B **61**, 2146 (2000).

[25] Martin Plihal, David C. Langreth, and Peter Nordlander, Phys. Rev. B **61**, R13341 (2000).

[26] Avraham Schiller and Selman Hershfield, Phys. Rev. B **62**, R16271 (2000).

[27] P. Coleman, C. Hooley, Y. Avishai, Y. Goldin, and A.F. Ho, J. Phys.: Condens. Matter **14**, 205 (2002).

[28] M.A. Cazalilla and J.B. Marston, Phys. Rev. Lett. **88**, 256403 (2002).

[29] S. Sasaki, S. De Franceschi, J.M. Elzerman, W.G. van der Wiel, M. Eto, S. Tarucha, and L.P. Kouwenhoven, Nature (London) **405**, 764 (2000); M. Eto and Yu.V. Nazarov, Phys. Rev. Lett. **85**, 1306 (2000); M. Pustilnik, Y. Avishai, and K. Kikoin, *ibid.* **84**, 1756 (2000); D. Giuliano and A. Tagliacozzo, *ibid.* **84**, 4677 (2000); C. Tejedor and L. Martin-Moreno, Phys. Rev. B **63**, 035319 (2001).

[30] U. Gerland, J. von Delft, T.A. Costi, and Y. Oreg, Phys. Rev. Lett. **84**, 3710 (2000); Yang Ji, M. Heiblum, D. Sprinzak, D. Mahalu, and Hadas Shtrikman, Science (Washington, DC, U.S.) **290**, 779 (2000).

[31] Jiwoong Park, Abhay N. Pasupathy, Jonas I. Goldsmith, Connie Chang, Yuval Yaish, Jason R. Petta, Marie Rinkoski, James P. Sethna, Hector D. Abrua, Paul L. McEuen, and Daniel C. Ralph, Nature (London) **417**, 722 (2002).

[32] Wenjie Liang, Matthew P. Shores, Marc Bockrath, Jeffrey R. Long, and Hongkun Park, Nature (London) **417**, 725 (2002).

[33] J. Nygård, D.H. Cobden, and P.E. Lindelof, Nature (London) **408**, 342 (2000).

[34] H.C. Manoharan, C.P. Lutz, and D.M. Eigler, Nature (London) **403**, 512 (2000).

[35] J. Kroha, Adv. Solid State Phys. **40**, 216 (2000); G. Göppert and H. Grabert, Phys. Rev. B **64**, 033301 (2001); J. Kroha and A. Zawadowski, Phys. Rev. Lett. **88**, 176803 (2002).

[36] T.H. Oosterkamp, T. Fujisawa, W.G. van der Wiel, K. Ishibashi, R.V. Hijman, S. Tarucha, and L.P. Kouwenhoven, Nature (London) **395**, 873 (1998).

[37] T. Fujisawa, T.H. Oosterkamp, W.G. van der Wiel, B.W. Broer, R. Aguado, S. Tarucha, and L.P. Kouwenhoven, Science (Washington, DC, U.S.) **282**, 932 (1998).

[38] R.H. Blick, D. Pfannkuche, R.J. Haug, K.v. Klitzing, and K. Eberl, Phys. Rev. Lett. **80**, 4032 (1998); H. Qin, A.W. Holleitner, K. Eberl, and R.H. Blick, Phys. Rev. B **64**, 241302(R) (2001); A.W. Holleitner, C.R. Decker, H. Qin, K. Eberl, and R.H. Blick, Phys. Rev. Lett. **87**, 256802 (2001); Alexander W. Holleitner, Robert H. Blick, Andreas K. Hüttel, Karl Eberl, and Jörg P. Kotthaus, Science (Washington, DC, U.S.) **297**, 70 (2002).

[39] H. Jeong, A.M. Chang, and M.R. Melloch, Science (Washington, DC, U.S.) **293**, 2221 (2001).

[40] Tomosuke Aono, Mikio Eto, and Kiyoshi Kawamura, J. Phys. Soc. Jpn. **67**, 1860 (1998).

[41] Tomosuke Aono and Mikio Eto, Phys. Rev. B **63**, 125327 (2001).

[42] A. Georges and Y. Meir, Phys. Rev. Lett. **82**, 3508 (1999).

[43] C.A. Büsser, E.V. Anda, A.L. Lima, M.A. Davidovich, and G. Chiappe, Phys. Rev. B **62**, 9907 (2000); W. Izumida and O. Sakai, *ibid.* **62**, 10260 (2000).

[44] N. Andrei, Gergely T. Zimanyi, and Gerd Schön, Phys. Rev. B **60**, R5125 (1999).

[45] T. Ivanov, Europhys. Lett. **40**, 183 (1997).

[46] T. Pohjola, J. König, M.M. Salomaa, J. Schmid, H. Schoeller, and Gerd Schön, Europhys. Lett. **40**, 189 (1997); Teemu Pohjola, Daniel Boese, Jürgen König, Herbert Schoeller, and Gerd Schön, J. Low Temp. Phys. **118**, 391 (2000).

[47] Ramón Aguado and David C. Langreth, Phys. Rev. Lett. **85**, 1946 (2000).

[48] Rosa López, Ramón Aguado, and Gloria Platero, Phys. Rev. Lett. **89**, 136802 (2002).

[49] H. Keiter and J.C. Kimball, J. Appl. Phys. **42**, 1460 (1971); N. Grewe and H. Keiter, Phys. Rev. B **24**, 4420 (1981); Y. Kuramoto, Z. Phys. B: Condens. Matter **53**, 37 (1983); E. Müller-Hartmann, *ibid.* **57**, 281 (1984).

[50] See also, N.E. Bickers, Rev. Mod. Phys. **59**, 845 (1987), for a review.

[51] A.A. Abrikosov, Physics (Long Island City, N.Y.) **2**, 21 (1965).

[52] S.E. Barnes, J. Phys. F: Met. Phys. **6**, 1375 (1976); **7**, 2637 (1977).

[53] P. Coleman, Phys. Rev. B **29**, 3035 (1984).

[54] N. Read and D.M. Newns, J. Phys. C **16**, 3273 (1983); **16**, L1055 (1983); Adv. Phys. **36**, 799 (1988).

[55] N. Read, J. Phys. C **18**, 2651 (1985); P. Coleman, J. Magn. Magn. Mater. **47**, 323 (1985).

[56] G. Baym and L.P. Kadanoff, Phys. Rev. **124**, 287 (1961); G. Baym, *ibid.* **127**, 1391 (1962).

[57] T.A. Costi, J. Kroha, and P. Wölfle, Phys. Rev. B **53**, 1850 (1996).

[58] D.L. Cox and A. Zawadowski, Adv. Phys. **47**, 599 (1998).

[59] A theory which corrects this deficiency is developed in J. Kroha, P. Wölfle, and T.A. Costi, Phys. Rev. Lett. **79**, 261 (1997); J. Kroha and P. Wölfle, Adv. Solid State Phys. **39**, 271 (1999).

[60] Th. Pruschke and N. Grewe, Z. Phys. B: Condens. Matter **74**, 439 (1989); D. Gerace, E. Pavarini, and L.C. Andreani, Phys. Rev. B **65**, 155331 (2002).

[61] K. Haule, S. Kirchner, J. Kroha, and P. Wölfle, Phys. Rev. B **64**, 155111 (2001).

[62] David C. Langreth and Peter Nordlander, Phys. Rev. B **43**, 2541 (1991).

[63] Hongxiao Shao, David C. Langreth, and Peter Nordlander, Phys. Rev. B **49**, 13929 (1994).

[64] T. Brunner and D.C. Langreth, Phys. Rev. B **55**, 2578 (1997).

[65] Takeshi Inoshita, Yoshio Kuramoto, and Hiroyuki Sakaki, Superlattices Microstruct. **22**, 75 (1997).

[66] Tae-Suk Kim and S. Hershfield, Phys. Rev. B **63**, 245326 (2001).

[67] Eran Lebanon and Avraham Schiller, Phys. Rev. B **65**, 035308 (2002).

[68] Matthias H. Hettler, Johann Kroha, and Selman Hershfield, Phys. Rev. Lett. **73**, 1967 (1994); Phys. Rev. B **58**, 5649 (1998).

[69] M. Plihal and David C. Langreth, Phys. Rev. B **60**, 5969 (1999).

[70] Martin Plihal, David C. Langreth, and Peter Nordlander, Phys. Rev. B **59**, 13322 (1999).

[71] M. Plihal and J.W. Gadzuk, Phys. Rev. B **63**, 085404 (2001).

[72] Peter Nordlander, Michael Pustilnik, Yigal Meir, Ned S. Wingreen, and David C. Langreth, Phys. Rev. Lett. **83**, 808 (1999).

[73] A. Rosch, J. Kroha, and P. Wölfle, Phys. Rev. Lett. **87**, 156802 (2001).

[74] This is not the only physical realization of a double quantum dot. For instance, it is possible to reach the opposite limit, large interdot interaction, by using a floating interdot capacitor. See, I.H. Chan, R.M. Westervelt, K.D. Maranowski, and A.C. Gossard, Appl. Phys. Lett. **80**, 1818 (2002).

[75] L.P. Kadanoff and G. Baym, *Quantum Statistical Mechanics* (Benjamin, New York, 1962).

[76] D.C. Langreth, in *Linear and Nonlinear Electron Transport in Solids*, Vol. 17 of *NATO Advanced Studies Institute, Series B: Physics*, edited by J.T. Devreese and V. E. Van Doren (Plenum, New York, 1976).

[77] It is not always true that a static voltage preserves time-translational invariance. In nonlinear systems driven away from equilibrium by a static voltage, one can have situations where at the stability limit of the stationary state a bifurcation to a time-dependent solution, which spontaneously breaks the time-translational symmetry, does develoP. See, for instance, M. Büttiker and H. Thomas, Z. Phys. B **34**, 301 (1979).

[78] For a general discussion see, M.P. Shaw, V.V. Mitin, E. Schöll, and H.L. Grubin, *The Physics of Instabilities in Solid State Electron Devices* (Plenum Press, New York, 1992).

[79] Vertex corrections are $O(1/N^2)$, see Ref. 53, which makes the NCA approximation correct to order $O(1/N)$.

[80] Wolfgang B. Thimm, Johann Kroha, and Jan von Delft, Phys. Rev. Lett. **82**, 2143 (1999).

[81] Aashish A. Clerk, Vinay Ambegaokar, and Selman Hershfield, Phys. Rev. B **61**, 3555 (2000).

[82] Y. Meir and Ned S. Wingreen, Phys. Rev. Lett. **68**, 2512 (1992).

[83] Qing-feng Sun and Hong Guo, Phys. Rev. B **64**, 153306 (2001).

[84] S. De Franceschi, R. Hanson, W.G. van der Wiel, J.M. Elzerman, J.J. Wijpkema, T. Fujisawa, S. Tarucha, and L.P. Kouwenhoven, Phys. Rev. Lett. **89**, 156801 (2002).

[85] Here, we focus on a projection procedure which is valid for diagonal (in the left/right index sense) operators. As we mentioned in Sec. IV A, we can construct a fully self-consistent NCA theory to order $O(1/N)$ by just including diagonal propagators/self-energies.